Fourier Analysis and Loss Modeling for Inductive Wireless Electric Vehicle Charging with Reduced Stray Field

Andrew Foote, *Student Member, IEEE,* Daniel Costinett, *Senior Member, IEEE,* Ruediger Kusch, *Senior Member, IEEE,* Mostak Mohammad, *Senior Member, IEEE,* and Omer Onar, *Senior Member, IEEE*

***Abstract*—With the growth of electric vehicle (EV) popularity, different charging options to increase user convenience and reduce charging times are being considered and researched. Among these, inductive wireless power transfer (WPT) systems for EVs are being designed to meet specifications such as stray field, power level, efficiency, misalignment tolerance, and ground clearance, which are all heavily influenced by the coil geometry. The proposed Fourier Analysis Method (FAM) is an analytical method to directly design coil geometries to meet stray field and power level requirements through an optimization of Fourier basis function coefficients. The outputs of the optimization are complex, planar coil geometries that meet the power level and stray field constraints with minimized loss factors. Contours of these potentials determine the coil conductor paths and loss models predict the system efficiency and performance over misalignment. The Fourier representation of the geometry is used to conveniently calculate the coupling over misalignment, external proximity effect loss, and ferrite loss. A 6.6 kW prototype WPT system with low stray field and high efficiency is built from the optimization results to validate the models and showcase the usefulness of the FAM design approach.**

***Index Terms*—wireless power transfer, inductive power transmission, coil design, electric vehicles, Fourier analysis**

Andrew Foote is the corresponding author of this work. Email: afoote5@vols.utk.edu; Phone: +1-650-496-7047; Mailing Address: 2704 Cherokee Farm Way, Suite 201, Knoxville, TN 37920 USA

Daniel Costinett is at the University of Tennessee, Knoxville Department of Electrical Engineering and Computer Science, 1520 Middle Dr, Knoxville, TN 37996 USA.

Ruediger Kusch is with Volkswagen Group Components, Berliner Ring 2, Building E111, 38436 Wolfsburg, Germany.

Mostak Mohammad and Omer Onar are with Oak Ridge National Laboratory, 2360 Cherahala Blvd, Knoxville, TN 37932 USA.

Parts of this work were first published in IEEE COMPEL 2020 [1]. This paper significantly adds to the previous publication by detailing loss and misalignment models validating experimentally with a new 6.6 kW coil. Parts of this work are also published in a dissertation [2].

This work was funded by Volkswagen Group Innovation in collaboration with the CURENT Engineering Research Center at the University of Tennessee, Knoxville and the Power Electronics and Electric Machinery Research Center at Oak Ridge National Laboratory.

This work made use of the Engineering Research Center Shared Facilities supported by the Engineering Research Center Program of the National Science Foundation and DOE under NSF Award Number EEC-1041877 and the CURENT Industry Partnership Program. Any opinions, findings and conclusions or recommendations expressed in this material are those of the authors and do not necessarily reflect those of the National Science Foundation.

I. Introduction

INDUCTIVE wireless power transfer (WPT) is useful in a variety of applications including the automotive and transportation sectors. WPT is a safe, convenient, flexible, and efficient charging solution that can easily be automated. The design of WPT systems to meet specifications such as power level, coupling, airgap, misalignment tolerance, stray field, and efficiency requires the computation of the fields, coupling, and inductances of various coil geometries. In particular, meeting the 15 µT pacemaker limit or the 27 µT ICNIRP 2010 public exposure magnetic field limit at the nominal WPT frequency of 85 kHz [3] and radiated EMI field limits in CISPR 11 [4] depends heavily on the coil geometry. More complex coil geometries such as bipolar coils and coils with shielding turns have been demonstrated to achieve higher power levels under stray field limits [5], [6]. Integrating shielding turns into the coil geometry design has several advantages over adding conductive or magnetic materials around the coil area to reduce stray field. In [7], [8], many Litz wire shielding turn designs were more efficient than copper ring shields or shielding plates of aluminum. In [9], eddy-current shielding with aluminum sheets was shown to actually increase stray field for bipolar coil geometries. Likewise, adding ferrite teeth [10], aluminum sheets, or ferrite outside the coil geometry [9] decreases the mechanical airgap of the system or increases the effective coil area and weight.

Attempting to consider a wider range of coil geometries including shielding turns, as well as other design parameters such as ferrite thicknesses, number of turns, and conductor types, results in a large design space. With the rising number of iterations needed, optimization based on brute-force iteration in FEA with full or partial 3D-modeling similar to [5] become increasingly computationally expensive. Likewise, many analytical methods like [6], [7] are pertinent only to circular or rectangular coils and are not general enough to model a large variety of possible geometries and aspect ratios. This limitation is also present in ferrite [11] and external proximity effect loss models [12].

To address these issues, this work applies Fourier analysis to WPT coil design and loss modeling. Magnetic component modeling and optimization using Fourier basis functions is already well-known in the design of magnetic resonance imaging (MRI) gradient coils [13], [14], fusion devices [15], and electric machines [16], [17]. In these works, basis functions, objectives, and constraints are added to regularize each coil design problem as an optimization to converge to a unique, optimal solution. For example, [14] receives a desired MRI gradient field distribution at a distance and iterates over basis function spaces to optimize for objectives such as minimum power dissipation, stored energy, and maximum current density. In these works, Fourier basis functions were shown to be well suited for symmetrical coil geometries and take advantage of symmetry to reduce matrix sizes, number of iterations, and overall computational times compared to other types of basis functions.

In the field of inductive wireless power transfer, Fourier analysis has been used to analytically calculate fields and mutual inductance of coils, but not to optimize coil designs including loss calculations. In [18], it is used to analyze circular and rectangular filament coils backed by magnetic or conductive media and predict mutual inductance. Similar modeling is used to model closely spaced rectangular coils in [19]. These works showcase the applicability of Fourier functions and analysis to model WPT coil geometries. Furthermore, many of the common types of WPT coil geometries are symmetric such as circular, rectangular, and bipolar geometries.

This work instead applies Fourier basis functions and analysis to optimize coil geometries to meet objectives of minimized current or loss factor under constraints of power level, stray field, and coil dimensions. The optimized geometry is implemented in a discretized coil design by selecting the ferrite and litz wire with the loss models. This work extends the Fourier Analysis Method (FAM) coil design method first published in [1] by adding loss and misalignment models. The methodology is experimentally validated with a 6.6 kW prototype including efficiency and field measurements over different airgaps and alignments.

The remainder of this work is organized as follows: Section II details the Fourier Analysis Method (FAM) for coil design optimization. Section III describes a misalignment model for translational and rotational misalignment and the application of loss models to the FAM including external proximity effect, ferrite losses, and others. To validate these models, the experimental results of a 6.6 kW prototype are given in Section IV. Finally, comparisons of this prototype with the literature are summarized in Table VII and conclusions are given in Section V.

II. The Fourier Analysis Method

The Fourier Analysis Method (FAM) is an analytical method to directly design coil geometries through an optimization of Fourier basis function coefficients to meet specifications such as power level, coil dimension, and stray field. The use of Fourier basis functions allows rapid computation of the currents, field, and coupling of a wide range of symmetric coil shapes. The outputs of the optimization are the magnetic scalar potentials of coil geometries that meet the power, stray field, and dimensional constraints with minimum current magnitude. This loss factor corresponds to the total amount of loss in the geometry. This first optimization step of the FAM design process in Fig. 1(a) is an inverse design step that directly optimizes the coil geometry from the input parameters by iterating the weights of the Fourier basis functions to minimize the loss factor objective function within the constraints. The optimization outputs are then used to flexibly determine coil conductor paths and adjust the impedance of the coils for varying numbers of turns without changing the overall coil shape. Afterwards, the number of turns is added to the Litz wire type, ferrite thickness and losses are calculated over misalignment to compare options and finally select the design.

In comparison, Fig. 1(b) summarizes the conventional coil design approaches that sweep over geometric parameters and evaluate the stray field and loss of each combination. Compared to three-dimensional FEA-based design methods like [5], the FAM is a two-dimensional approach, much less computationally complex, and faster. Compared to most analytical design methods like [6], [7], the FAM is more general and can analyze much more complex symmetric geometries than circular or rectangular coils. With these benefits, the FAM enables a more generalized coil design methodology that rapidly evaluates complex symmetric coil shapes, broadening the scope of design optimization for WPT systems.

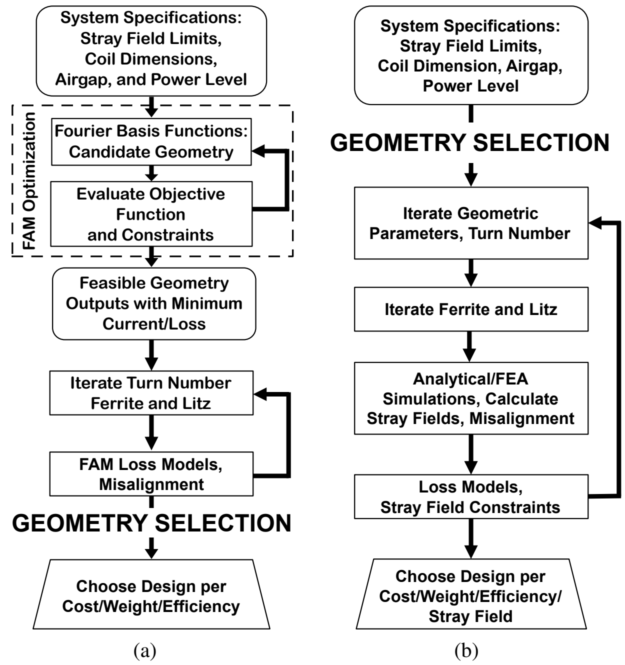

Fig. 1. Comparison of the Fourier Analysis Method (FAM) design process and a conventional design process. (a) The FAM design process where complex coil geometries are generated to meet the stray field limit with minimum current or loss factors through an optimization of Fourier basis function coefficients. The number of turns and coil materials are then iterated to evaluate loss for the candidate geometries. (b) A conventional design process similar to [5], [6], [7] where geometric parameters are chosen and swept using FEA or analytical methods. Each parameter combination is evaluated for stray field and loss.

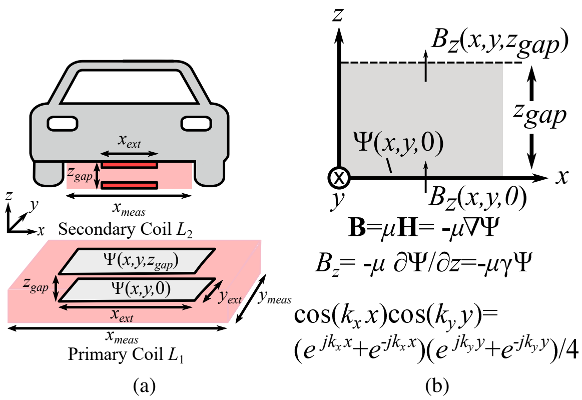

Fig. 2. (a) Illustration of the EV WPT system defined by coil outer dimensions of x_{ext} and y_{ext}, system airgap z_{gap}, stray field limits outside a region with dimensions of x_{meas} and y_{meas}, and magnetic scalar potential Ψ used in the Fourier Analysis Method (FAM). (b) FAM axes layout and key equations.

The overall WPT system layout used in FAM is illustrated in Fig. 2 where the outer dimensions of the primary and secondary coils are x_{ext} and y_{ext}, the outer dimensions of the region for stray-field measurement are x_{meas} and y_{meas}, and the magnetic scalar potential is Ψ. In the FAM, the four different basis functions are combinations of cosine and sine functions in the x and y-directions. Examples of the four selected functions, $\cos x \cos y$, $\sin x \cos y$, $\cos x \sin y$, and $\sin x \sin y$, are shown in Fig. 3. The $\cos x \cos y$ set corresponds to circular or rectangular geometries, the $\sin x \cos y$ and $\cos x \sin y$ sets correspond to bipolar geometries, and the $\sin x \sin y$ set corresponds to quadrupole geometries. As first detailed in [1], each function is defined by k_x and k_y, the spatial wavenumbers in units of radians per meter in the x and y-directions, respectively. These wavenumbers are $k_x(m) = 2\pi m/D_x$ and $k_y(n) = 2\pi n/D_y$ for integer m and n from $-N+1$ to $N-1$, where D_x and D_y are design space dimensions greater than the desired coil extents. N defines the highest frequency basis functions considered in each direction, $k_x(N) = 2\pi N/D_x$ and $k_y(N) = 2\pi N/D_y$ in the x and y-directions, respectively. For most geometries with extents around half of D_x and D_y, N =15 is adequate and the coefficients of the higher frequency basis functions are nearly zero. The coefficients of the four basis functions are a $N \times N \times 4$ matrix with each $N \times N \times 1$ matrix representing the first quadrant of each of the sets of basis functions with m and n from 0 to $N-1$ with coefficients $\psi(k_x, k_y)$ at each pair of wavenumbers. To compute the full Fourier-domain matrix of the coil shape, each $N \times N \times 1$ matrix is reflected to the corresponding negative wavenumber components according to the symmetry conditions of Fig. 3(a) to create a $(2N-1) \times (2N-1)$ matrix. The summation of these matrices yields the total Fourier domain coefficients $\psi(m,n)$ across both negative and positive k_x and k_y. The scalar magnetic potential in the spatial domain, $\Psi(x,y,z)$, is the inverse Discrete Fourier Transform (IDFT) of this matrix,

$$\Psi(x,y,z) = \sum_{m,n=-N+1}^{N-1}\sum^{N-1} \psi(m,n)e^{j(k_x x + k_y y + k_z z)}/4 \quad (1)$$

which can be rapidly computed by conventional Fast Fourier Transform algorithms.

For ferrite-backed coils, the potential of the coil surface is defined by the surface current boundary condition

$$\boldsymbol{K} = \nabla \times \hat{k}\Psi = \frac{\partial \Psi}{\partial y}\hat{i} - \frac{\partial \Psi}{\partial x}\hat{j} \quad (2)$$

where $\hat{i}$, $\hat{j}$, and $\hat{k}$ are unit vectors in the x, y, and z directions, respectively, and $\boldsymbol{K}$ is the surface current vector. This assumes the change in the magnetic potential and field in the ferrite are close to zero due to the low reluctance of the ferrite compared to the airgap. The surface currents in the x and y-direction, K_x and K_y, are then

$$K_x(x,y,0) = \sum_{m,n=-N+1}^{N-1}\sum^{N-1} jk_y\psi(m,n)e^{j(k_x x + k_y y)}/4 \quad (3)$$

$$K_y(x,y,0) = \sum_{m,n=-N+1}^{N-1}\sum^{N-1} -jk_x\psi(m,n)e^{j(k_x x + k_y y)}/4. \quad (4)$$

This surface current representation allows for the coil geometry to be analyzed as a surface current density independent from the number of turns. To determine the coil conductor paths and current, the surface currents are grouped by dividing the net change of potential into a number of turns N_T. The number of turns can be adapted to flexibly change the impedance of the coils to meet various driving voltages and loads. This results in the RMS current in each turn: I_1 for the primary or transmitter coil, and I_2 for the secondary or receiver coil,

$$I_1 = (\max \Psi(x,y,0) - \min \Psi(x,y,0))/N_T. \quad (5)$$

The conductor paths are the contours of the potential at values

$$C = \min \Psi(x,y,0) + \left(0 : (N_T - 1) + \frac{1}{2}\right) I_1. \quad (6)$$

As in [1], the number of turns are limited by the outer diameter of the gauge of wire, d_{out}, and the maximum current density, K_{max}, by

$$\frac{\max \Psi(x,y,0) - \min \Psi(x,y,0))}{N_T d_{out}} = \frac{I_1}{d_{out}} < K_{max} \quad (7)$$

so that the geometries fit in a single winding layer.

In the Fourier domain, the potential Ψ is differentiated to obtain algebraic relationships between the potential and the field $\boldsymbol{B}$,

$$\boldsymbol{B} = \mu_0 \boldsymbol{H} = -\mu_0 \nabla \Psi. \quad (8)$$

Neglecting displacement current in quasi-magnetostatic conditions, the wavenumber in the z-direction, k_z, is derived by observing that $\nabla \times \boldsymbol{B} = 0$ in the absence of airgap currents. Here, it is assumed there are no conductors or volume currents between the primary and secondary coils with only air in the airgap. Combined with $\nabla \cdot \boldsymbol{B} = 0$, the field and potential satisfy

$$\nabla^2 \Psi = \nabla^2 \boldsymbol{B} = 0. \quad (9)$$

This article has been accepted for publication in IEEE Transactions on Transportation Electrification. This is the author's version which has not been fully edited and content may change prior to final publication. Citation information: DOI 10.1109/TTE.2024.3363612

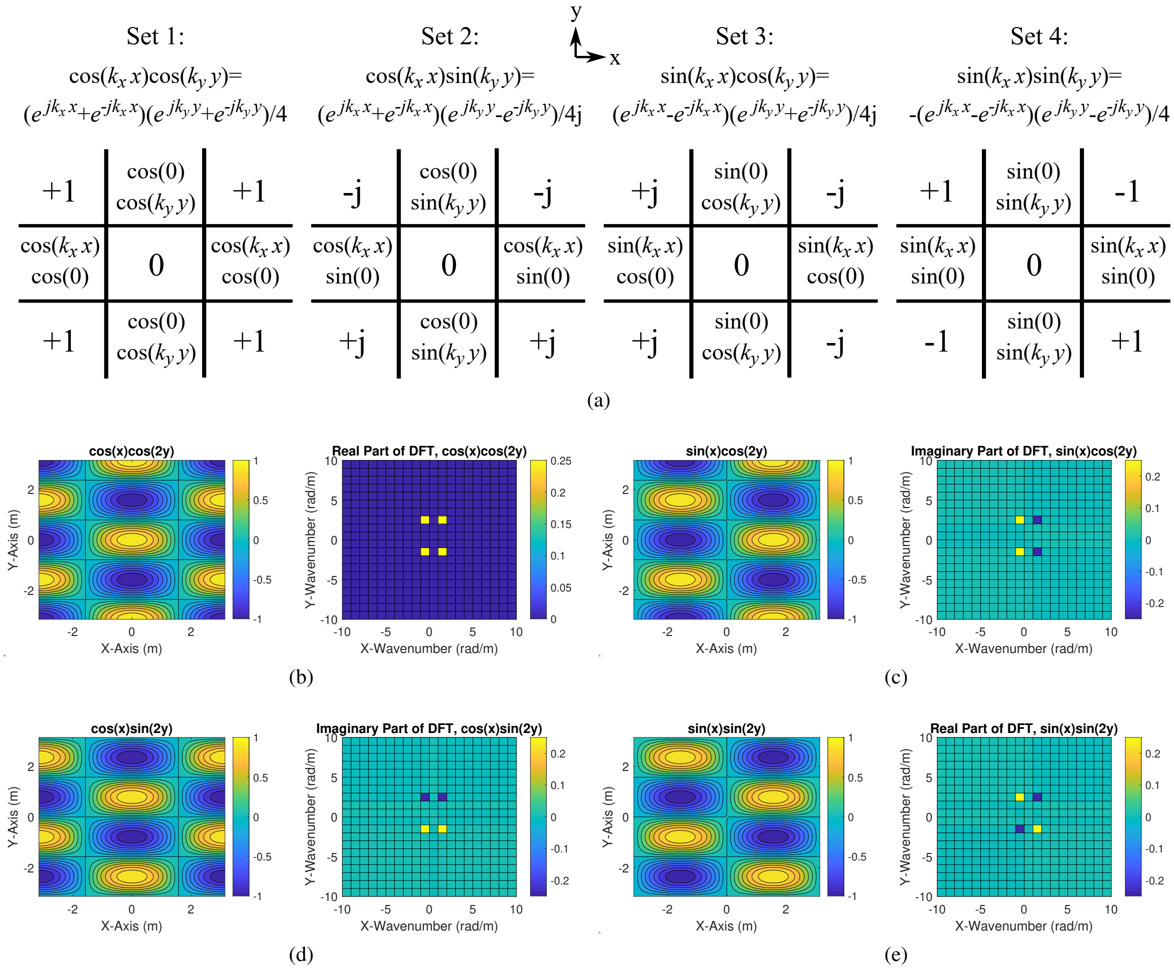

Fig. 3. Diagrams of the 4 basis functions sets considered in the Fourier Analysis Method. (a) The symmetry conditions for each basis function set comprised of real and complex conjugate relationships. With these relationships, each basis function can be represented by one value in the first quadrant, limiting the number of variables and constraints needed in the optimization function. (b) Example of a $\cos x \cos y$ basis function. (c) Example of a $\sin x \cos y$ basis function. (d) Example of a $\cos x \sin y$ basis function. (e) Example of a $\sin x \sin y$ basis function.

Therefore, when real, non-zero wavenumbers exist in the x and y-directions, k_z is imaginary and is

$$k_z = \pm\sqrt{-k_x^2 - k_y^2} = \pm j\gamma, \tag{10}$$

where $\gamma = \sqrt{k_x^2 + k_y^2}$, and the magnetic potential in the airgap must satisfy

$$\frac{\partial^2 \Psi}{\partial z^2} - k_z^2 \Psi = 0 \tag{11}$$

which has solution

$$\Psi(z) = c_1 e^{-\gamma z} + c_2 e^{\gamma z}. \tag{12}$$

The constants c_1 and c_2 are found using the boundary conditions at $\Psi(0)$ and $\Psi(z_{gap})$, yielding the relationship [16],

$$\Psi(z) = \frac{\sinh \gamma z}{\sinh \gamma z_{gap}} \Psi(z_{gap}) - \frac{\sinh \gamma (z - z_{gap})}{\sinh \gamma z_{gap}} \Psi(0). \tag{13}$$

By (9)–(13), coils with potentials with higher k_x and k_y, i.e. with shorter wavelengths, will consist of components that have higher k_z or γ and decay faster in the z-direction than those with more lower k_x and k_y potentials. This scattering relationship describes how coils with larger diameters have fields that decay slower away from the coil surface than those of smaller coils. An example of this for a rectangular primary coil is shown in Fig. 4. At the surface of the coil, the DFT of the potential and discretized potential are shown in Fig. 4(a)-4(b). The z-field at the surface of the coil by (16) is given in Fig. 4(c)-4(d). The z-field from the primary at the surface of the secondary at z_{gap} is shown in Fig. 4(e)-4(f), where only the low-frequency components of the field are largely remaining. By combining (8) with (13), the fields at z are a function of z_{gap} and γ for ferrite-backed coils with single-sided flux generation

$$B_x(x, y, z) = \sum_{m,n=-N+1}^{N-1} \sum^{N-1} \frac{-\mu_0 j k_x \psi(m, n) e^{j(k_x x + k_y y)}}{4} \cdot \frac{\sinh \gamma (z - z_{gap})}{\sinh \gamma z_{gap}} \tag{14}$$

This article has been accepted for publication in IEEE Transactions on Transportation Electrification. This is the author's version which has not been fully edited and content may change prior to final publication. Citation information: DOI 10.1109/TTE.2024.3363612

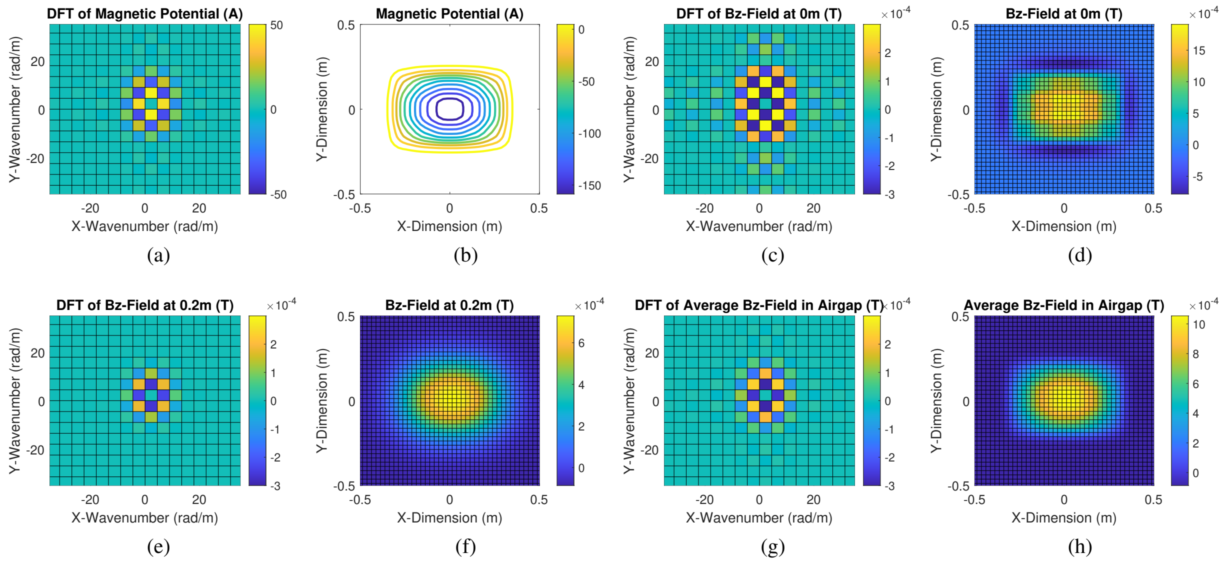

Fig. 4. Example potentials and field of a rectangular coil when $z_{gap} = 0.2$ m. (a) DFT and (b) contours of the magnetic scalar potential. (c) DFT and (d) discretized surface z-field at the surface of the primary coil. (e) DFT and (f) discretized z-field of the primary coil across the airgap at the surface of the secondary coil. (g) The DFT and (h) average of the z-field of the primary coil in the airgap.

$$B_y(x,y,z) = \sum_{m,n=-N+1}^{N-1}\sum^{N-1} \frac{-\mu_0 j k_y \psi(m,n) e^{j(k_x x + k_y y)}}{4} \cdot \frac{\sinh \gamma(z - z_{gap})}{\sinh \gamma z_{gap}} \quad (15)$$

$$B_z(x,y,z) = \sum_{m,n=-N+1}^{N-1}\sum^{N-1} \frac{-\mu_0 \gamma \psi(m,n) e^{j(k_x x + k_y y)}}{4} \cdot \frac{\cosh \gamma(z - z_{gap})}{\sinh \gamma z_{gap}}. \quad (16)$$

This calculation determines the fields from the primary coil only with $\Psi(z_{gap}) = 0$ and zero tangential field at the surface of the secondary ferrite. The fields from the secondary coil are calculated in a similar manner and added to the primary fields to obtain the total field in the air gap by superposition.

The average of the fields in the airgap are also conveniently obtained by this representation. The average field is derived by integrating the contribution from each basis function from $z = 0$ to z_{gap} and dividing by z_{gap} to obtain the average field in the airgap,

$$B_{x,avg}(x,y) = \sum_{m,n=-N+1}^{N-1}\sum^{N-1} \frac{-\mu_0 j k_x \psi(m,n) e^{j(k_x x + k_y y)}}{\gamma z_{gap} \sinh \gamma z_{gap}} \cdot (\cosh \gamma z_{gap} - 1) \quad (17)$$

$$B_{y,avg}(x,y) = \sum_{m,n=-N+1}^{N-1}\sum^{N-1} \frac{-\mu_0 j k_y \psi(m,n) e^{j(k_x x + k_y y)}}{\gamma z_{gap} \sinh \gamma z_{gap}} \cdot (\cosh \gamma z_{gap} - 1) \quad (18)$$

$$B_{z,avg}(x,y) = \sum_{m,n=-N+1}^{N-1}\sum^{N-1} \frac{-\mu_0 \gamma \psi(m,n) e^{j(k_x x + k_y y)}}{\gamma z_{gap}}. \quad (19)$$

The average field magnitude in the airgap, $B_{avg}(x,y)$, is then

$$B_{avg}(x,y) = \sqrt{B_{x,avg}(x,y)^2 + B_{y,avg}(x,y)^2 + B_{z,avg}(x,y)^2}. \quad (20)$$

The computation of the field at the surface of the coils allows for the computation of the coupling coefficient k, as detailed in [1], assuming matched couplers and currents as

$$k = \frac{E_m(\psi)}{2E_s(\psi)} = \frac{M I_1 I_2}{\frac{1}{2}L_1 I_1^2 + \frac{1}{2}L_2 I_2^2} = \frac{\int_\Omega \Psi(x,y,0) B_z(x,y,z_{gap}) d\Omega}{\int_\Omega \Psi(x,y,0) B_z(x,y,0) d\Omega}, \quad (21)$$

where E_s is the self magnetic energy of each coil individually, E_m is the mutual magnetic energy between the coils, M is the mutual inductance, and L_1 and L_2 are the self inductances.

A. Optimization of Stray Field and Current

Using the FAM framework, an optimization is formulated and solved to design coil geometries to minimize the loss factor $\Gamma^2_{K,Loss}$ for a fixed power level when bounded by coil extents at x_{ext} and y_{ext} and field limits at the measurement extents x_{meas} and y_{meas}. For this optimization, the dimensions of the design space are $D_x = D_y = 1.4$ m with a resolution of 2 cm.

$\Gamma_{K,Loss}(\psi)$ corresponds with the total current magnitude in the coil geometry defined by

$$\Gamma^2_{K,Loss}(\psi) = \int_\Omega K(x,y,0)^2 d\Omega = (||K_x(\psi)||_2^2 + ||K_y(\psi)||_2^2)/16. \quad (22)$$

This is quickly calculated in the Fourier domain from the basis function coefficients by noting that the Fourier transform is a unitary function. This avoids the computation of $K(x, y, 0)$ in each objective function evaluation step. The integral of the current density squared multiplied by the equivalent resistance of the coil surface area is the coil conduction loss. The squared current integral is used as the loss factor because it is only a function of the geometry and is not dependent on the selection of the number of turns and conductors chosen later in the design process.

The objective function is formulated as the minimization of the loss factor $\Gamma^2_{K,Loss}$ added to the 1-norm of the magnitude of the basis function coefficients to eliminate small values of zero-valued basis functions such as $\sin 0 \cos y$ yielding the objective function

$$\frac{\Gamma^2_{K,Loss}(\psi)}{P} + \alpha \frac{||\psi||_1}{P} \tag{23}$$

where $\alpha = 0.1$ to minimize the weight of the zero-valued functions compared to the normalized loss factor and P is the desired coil-coil power level.

Constraints are imposed on the optimization to achieve a specified power level, a stray field level, and coil dimensions or extents. The first constraint is the coil-coil power transfer,

$$(P - 2\pi f E_m(\psi))/P \leq 0. \tag{24}$$

The next constraint uses the maximum average stray field magnitude $B_{str,max}(\psi)$,

$$(B_{str,max}(\psi, x_{meas}, y_{meas}) - B_{str,lim})/B_{str,lim} \leq 0 \tag{25}$$

where

$$B_{str,max}(\psi, x_{meas}, y_{meas}) = ||B_{str,avg}(x, y)||_{50}. \tag{26}$$

The inclusion of stray field as a constraint incorporates the need to add shielding for compliance with safety standards for public magnetic field exposure and EMI standards. $B_{str,max}(\psi, x_{meas}, y_{meas})$ is computed as the 50-norm of the spatial stray-field matrix, $B_{str,avg}$, which approximates the infinity norm or the maximum value of the matrix. $B_{str,avg}$ is the average field magnitude over the z-direction of the airgap B_{avg} as in (20) outside the measurement extents x_{meas} and y_{meas}. The use of the average or 1-norm of the field across the airgap in the z-direction accounts for the stray fields in the entire airgap such as near the surface of the primary coil, at the middle of the airgap, and at the surface of the other coil across the airgap. A higher-order norm could also be used to approximate the maximum across the airgap in the z-direction, but the 1-norm results in a smoothed field matrix similar to the field at the middle of the airgap.

The third constraint limits the current density to the desired coil extents such that the surface integral of the stray current squared $\kappa^2_{str}(\psi, x_{ext}, y_{ext}) = \int_\Omega K_{str}(x, y, 0)^2 d\Omega$ outside the coil extents x_{ext} and y_{ext}, is a small percentage, $\beta = 10^{-4}$ of the surface integral of the total current squared $\Gamma^2_{K,Loss}(\psi)$.

$$\frac{\kappa^2_{str}(\psi, x_{ext}, y_{ext})}{\Gamma^2_{K,Loss}(\psi)} - \beta \leq 0 \tag{27}$$

This constraint is included to restrict the optimized coil geometry to the specified coil dimensions, x_{ext} and y_{ext}.

In summary, the objective function and constraints form the optimization

$$\begin{gathered} \min \left(\frac{\Gamma^2_{K,Loss}(\psi)}{P} + \alpha \frac{||\psi||_1}{P} \right) \\ \text{s.t.} \\ (P - 2\pi f E_m(\psi))/P \leq 0, \\ (B_{str,max}(\psi, x_{meas}, y_{meas}) - B_{str,lim})/B_{str,lim} \leq 0, \\ \frac{\kappa^2_{str}(\psi, x_{ext}, y_{ext})}{\Gamma^2_{K,Loss}(\psi)} - \beta \leq 0. \end{gathered} \tag{28}$$

This optimization was performed with the gradient-based fmincon optimizer in MATLAB. The results of this optimization are plotted in Fig. 5 for $B_{str,lim}$ of 5 µT to 1 mT with $x_{ext} = 0.7$ m and $y_{ext} = 0.5$ m, and with $x_{meas} = 0.7$ m and $y_{meas} = 0.5$ m [1]. This approximately 4:3 aspect ratio for the coils and measurement distance was chosen to show the flexibility of the method to handle a large number of coil shapes and sizes as most analytical methods focus on 1:1 square coils or circular coils. It also allows for a difference between the bipolar $\cos x \sin y$ and $\sin x \cos y$ basis function results. The misalignment range in the SAE J2954 standard [3], ± 10 cm and ± 7.5 cm, also supports this type of aspect ratio, as the misalignment performance of the x-direction must be better than that of the y-direction to support parking. Vehicle alignment is easier to adjust in the front and back direction relative to the side to side direction. The coil dimensions are set by the airgap and the measurement distances were chosen to be the coil extents to make the stray fields in the optimization higher magnitude.

Contours of the outputs at $B_{str,lim} = 20$ µT and 1 mT are shown in Fig. 6. As shown, when $B_{str,lim} = 1$ mT in the geometries are simple rectangular, bipolar or double-D, and quadrupole shapes limited by the extents of the coil in Fig. 6(a)-6(d). When constrained by $B_{str,lim} = 20$ µT, the geometries develop smaller poles and shielding structures that provide flux cancellation to reduce the field outside the stray field boundaries in Fig. 6(e)-6(h). The smaller poles reduce the coupling of the coils for the fixed airgap. Likewise, shielding structures slightly detract from the coupling and require additional current. These two factors increase the amount of current needed for a given amount of power for Fig. 6(e)-6(h) relative to the simpler structures of Fig. 6(a)-6(d). The coupling of the geometries decreases and the current required to achieve the 6.6 kW power level increases for the fixed coil extents and airgap.

Assuming matched currents in both coils, these results can be scaled to different power levels by multiplying the current density and fields of the solutions by the square root of the ratio of the desired power level and 6.6 kW. The optimization could also be run again with a different choice of power level P. To analyze the currents and fields of the geometries with unmatched current, such as when the system is operated with non-ideal loading or at different output powers with a fixed output voltage, the currents of each coil can be

This article has been accepted for publication in IEEE Transactions on Transportation Electrification. This is the author's version which has not been fully edited and content may change prior to final publication. Citation information: DOI 10.1109/TTE.2024.3363612

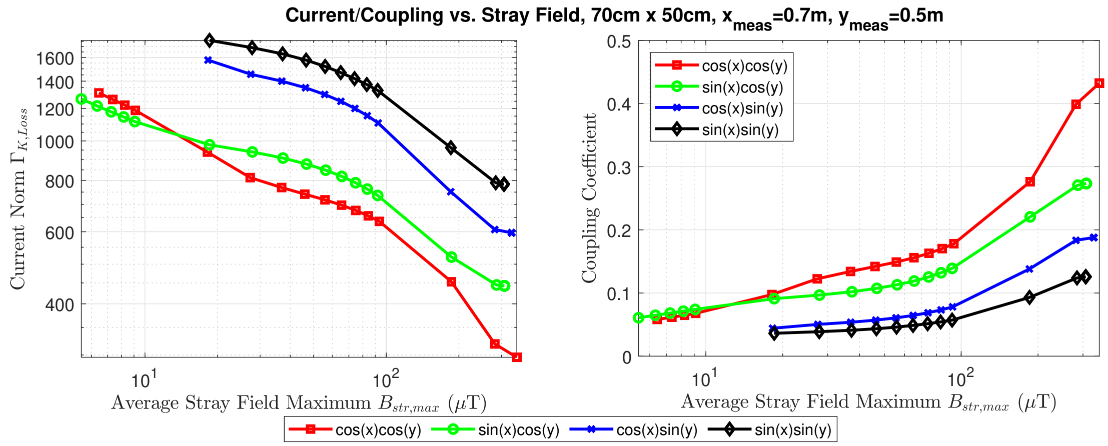

Fig. 5. Optimization Outputs: The maximum average stray field magnitude vs. the square root of the integral of the current magnitude squared at 6.6 kW and coupling coefficient at z_{gap} = 200 mm at alignment for x_{ext} = 0.7 m and y_{ext} = 0.5 m for $B_{str,lim}$ of 5 μT to 1 mT with x_{meas} = 0.7 m and y_{meas} = 0.5 m [1].

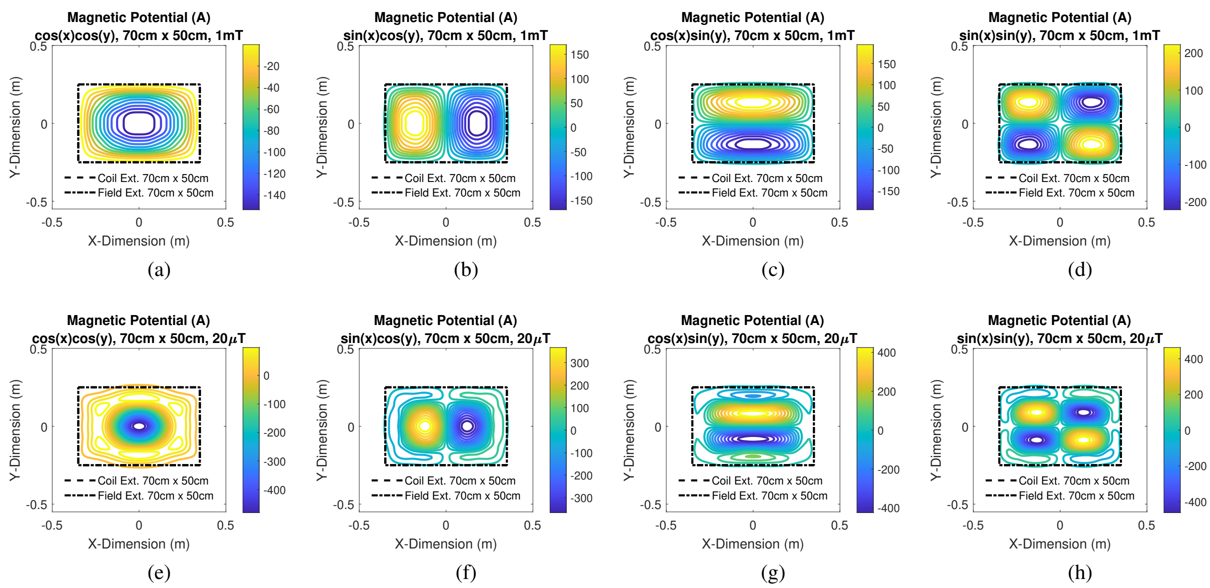

Fig. 6. Plots of coil contours from each basis function for x_{ext} = 0.7 m and y_{ext} = 0.5 m when constrained by $B_{str,lim}$ = 1 mT with x_{meas} = 0.7 m and y_{meas} = 0.5 m: (a) A rectangular coil from the $\cos x \cos y$ set with labeled extents and measurement distances. (b) A bipolar coil in the x-direction from the $\sin x \cos y$ set. (c) A bipolar coil in the y-direction from the $\cos x \sin y$ set. (d) A 4-pole coil from the $\sin x \sin y$ set. Plots when constrained by $B_{str,lim}$ = 20 μT: (e) A shielded rectangular coil from the $\cos x \cos y$ set. (f) A shielded bipolar coil in the x-direction from the $\sin x \cos y$ set. (g) A shielded bipolar coil in the y-direction from the $\cos x \sin y$ set. (h) A shielded quadrupole coil from the $\sin x \sin y$ set.

scaled separately, and the fields can be added together through superposition.

The best-performing coil designs depend on the values and aspect ratio of both the coil and field extents. Bipolar geometries perform better with their long-axis, or the direction over which the two poles lie, along larger coil extents and when more stray field is allowed on their long-axis. For example, the optimization outputs in Figs. 7-9 are with square coil extents x_{ext} = 0.6 m and y_{ext} = 0.6 m with a $B_{str,lim}$ of 3 μT to 200 μT at measurement extents of x_{meas} = 0.7 m and y_{meas} = 0.7 m and also for x_{meas} = 1.0 m and y_{meas} = 0.7 m. The stray field is lower than the previous optimization outputs in Fig. 5 as the measurement distances are slightly further away. For this optimization, $D_x = D_y$ = 1.4 m with a resolution of 2 cm.

As in Figs. 7 and 8, the $\sin x \cos y$ set performs well when the measurement extents are x_{meas} = 1.0 m and y_{meas} = 0.7 m and the stray field can be larger in the x-direction. Meanwhile, the $\sin x \cos y$ and $\cos x \sin y$ outputs are identical when the measurement extents are the same in both directions with x_{meas} = 0.7 m and y_{meas} = 0.7 m. In Fig. 7, the $\cos x \cos y$ outputs have the lowest current and highest coupling where the outputs are less constrained by stray field with high $B_{str,lim}$. As in Fig. 9, both the $\cos x \cos y$ and $\sin x \sin y$ outputs extend in the x-direction for x_{meas} = 1.0 m and y_{meas} = 0.7 m. Here, the $\sin x \sin y$ set does not converge below $B_{str,lim}$ = 20 μT.

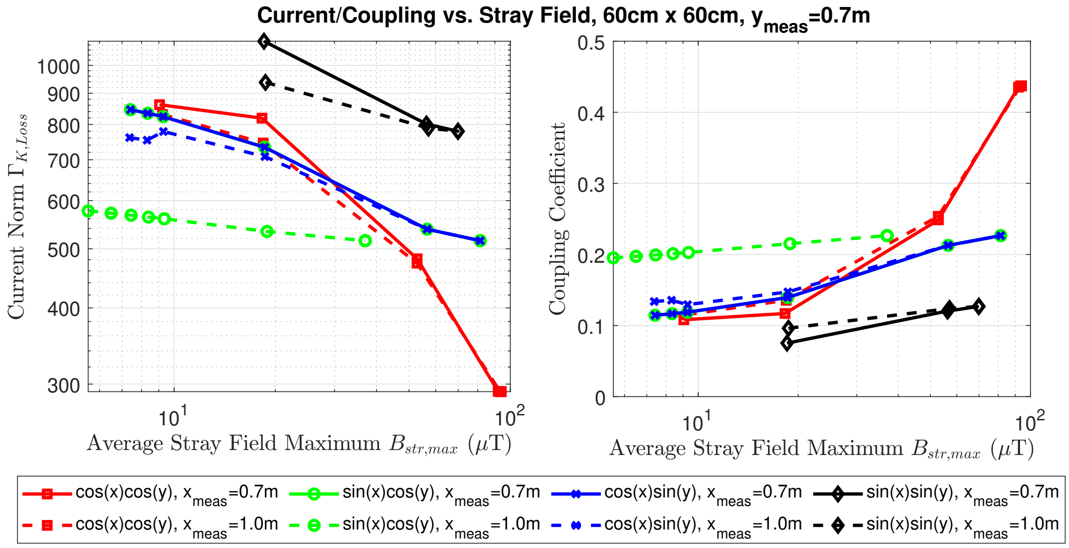

Fig. 7. Optimization Outputs: The maximum average stray field magnitude vs. the square root of the integral of the current magnitude squared at 6.6 kW and coupling coefficient at $z_{gap} = 200$ mm at alignment for $x_{ext} = 0.6$ m and $y_{ext} = 0.6$ m for $B_{str,lim}$ of 3 µT to 200 µT with $x_{meas} = 0.7$ m and $y_{meas} = 0.7$ m and $x_{meas} = 1.0$ m and $y_{meas} = 0.7$ m.

TABLE I
RECTANGULAR COIL GEOMETRY SWEEP PARAMETERS

Parameter	Min. (m)	Step (m)	Max. (m)	Points
Coil X-Dimension	0.2	0.1	0.7	6
Coil Y-Dimension	0.2	0.1	0.5	4
Winding Width	0.1	0.05	0.15	2
Airgap	0.2 m			
Ferrite Dimensions	1.4 m x 1.4 m			

B. Comparison to FEA Sweep of Rectangular Coils

In Fig. 10, the $\cos x \cos y$ FAM outputs in Figs. 5-6 are compared to a sweep of rectangular coil geometries in finite-element analysis (FEA) software. The FAM outputs are exported from FAM as discretized surface current densities and interpolated in FEA so that they could be compared in the same FEA setup. This sweep is similar to the approach of [5]. In Table I, the parameters of the simulations are shown. As seen, most of the FAM optimization outputs are on the Pareto front of the FEA rectangular geometry solutions. The FAM outputs are constrained by the selection of N, D_x, and D_y as they define the lowest and highest wavenumbers of basis functions used in the optimization. For this comparison, the stray field at the middle of the airgap was used as the comparison metric for ease of calculation in FEA instead of the average stray field for both the rectangular coil geometries and $\cos x \cos y$ outputs. On the same computer, the 3D FEA simulation took 2.4 minutes to simulate each geometry during the sweep of rectangular coils, while each FAM function evaluation, which evaluates a candidate geometry in the MATLAB fmincon optimizer for the objective function and constraints, averaged 3.7 ms. The desktop computer had an Intel Xeon C5-1620, 3.60 GHz, processor and 80 GB of RAM.

III. MISALIGNMENT AND LOSS MODELING

After the coil geometry is optimized, the misalignment performance and system efficiency can be evaluated to realize a physical design. The representation of the coil geometry in the Fourier domain can assist with several aspects of these calculations such as with calculating the coupling over misalignment and calculating the ferrite and wire loss which are dependent on the fields of the geometry. The loss models given here assume a series-series compensated system as realized in the experimental prototype.

A. Misalignment Model

The FAM can predict system performance in both translational and rotational misalignments by calculating the fields and mutual inductance of the system for misaligned conditions. For example, the efficiency over misalignment of the geometries of Fig. 16(a)-16(b) are given in Fig. 16(g)-16(h). In the Fourier domain, translational misalignment is modeled by adding phase-shift to the Fourier components, where x_{sft} and y_{sft} are the translational misalignment of the coil in the x-direction and y-direction respectively,

$$\psi_{sft}(m,n) = \psi(m,n)e^{(-k_x x_{sft} - k_y y_{sft})}. \tag{29}$$

An example of this operation for the selected geometry potential in Fig. 11(a) is shown in Fig. 11(c).

In a similar manner, rotation in the spatial domain produces rotation in the Fourier domain,

$$\begin{bmatrix} k'_x \\ k'_y \end{bmatrix} = \begin{bmatrix} \cos\theta_{sft} & -\sin\theta_{sft} \\ \sin\theta_{sft} & \cos\theta_{sft} \end{bmatrix} \begin{bmatrix} k_x \\ k_y \end{bmatrix} \tag{30}$$

where θ_{sft} is the rotational misalignment and k'_x and k'_y are the rotated wavenumbers. An example of this is shown in Fig. 11(b). Due to the limited number of basis functions used

This article has been accepted for publication in IEEE Transactions on Transportation Electrification. This is the author's version which has not been fully edited and content may change prior to final publication. Citation information: DOI 10.1109/TTE.2024.3363612

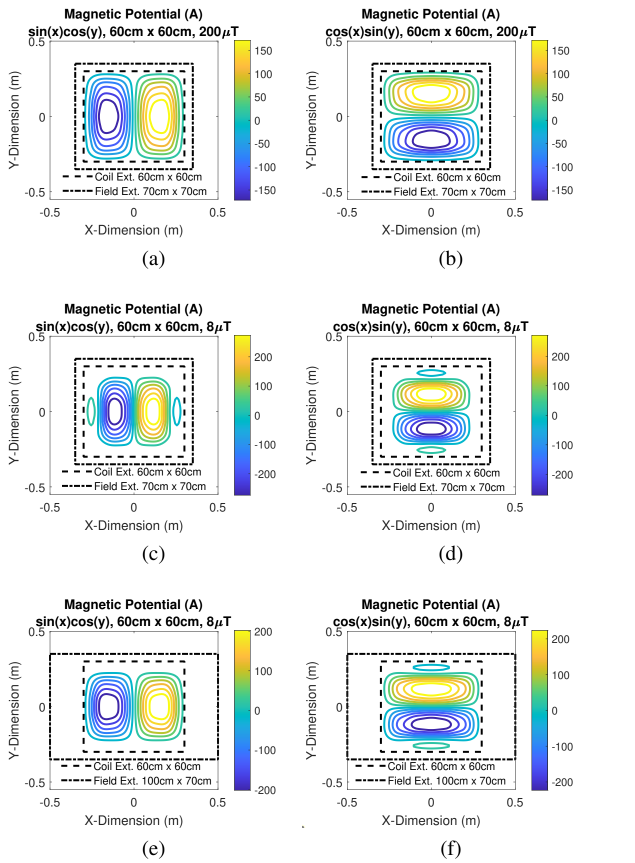

Fig. 8. Plots of coil contours from the $\sin x \cos y$ and $\cos x \sin y$ outputs with $x_{ext} = 0.6$ m and $y_{ext} = 0.6$ m. With $B_{str,lim} = 200$ μT with $x_{meas} = 0.7$ m and $y_{meas} = 0.7$ m: (a) A bipolar coil in the x-direction from the $\sin x \cos y$ set. (b) A bipolar coil in the y-direction from the $\cos x \sin y$ set. With $B_{str,lim} = 8$ μT with $x_{meas} = 0.7$ m and $y_{meas} = 0.7$ m: (c) A shielded bipolar coil in the x-direction from the $\sin x \cos y$ set. (d) A shielded bipolar coil from the $\cos x \sin y$ set. $B_{str,lim} = 8$ μT with $x_{meas} = 1.0$ m and $y_{meas} = 0.7$ m: (e) A shielded bipolar coil in the x-direction from the $\sin x \cos y$ set. (f) A shielded bipolar coil from the $\cos x \sin y$ set.

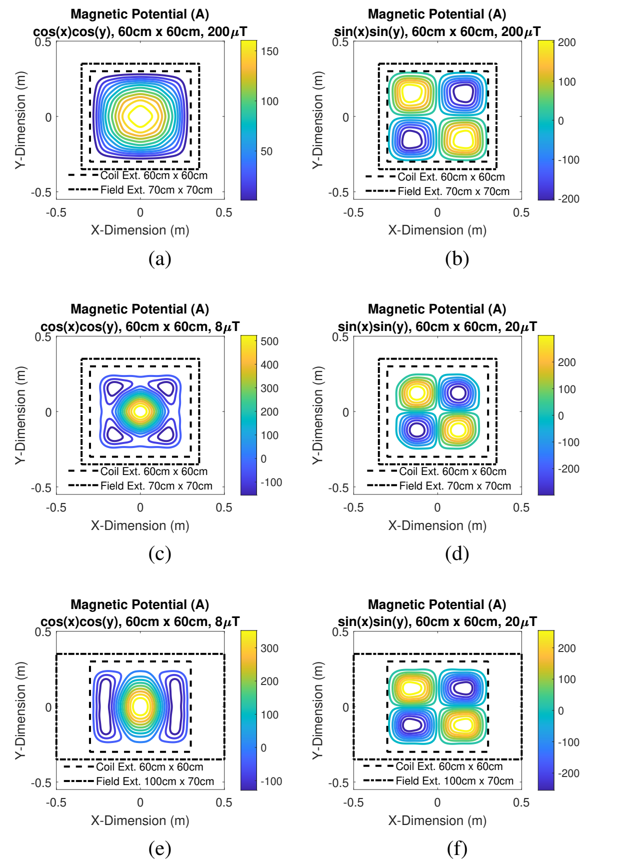

Fig. 9. Plots of coil contours from the $\cos x \cos y$ and $\sin x \sin y$ outputs with $x_{ext} = 0.6$ m and $y_{ext} = 0.6$ m. With $x_{meas} = 0.7$ m and $y_{meas} = 0.7$ m: (a) A square coil from the $\cos x \cos y$ set and (b) quadrupole coil from the $\sin x \sin y$ with $B_{str,lim} = 200$ μT. (c) A shielded circular coil from the $\cos x \cos y$ set with $B_{str,lim} = 8$ μT and (d) quadrupole coil from the $\sin x \sin y$ set with $B_{str,lim} = 20$ μT. With $x_{meas} = 1.0$ m and $y_{meas} = 0.7$ m: (e) A shielded circular coil from the $\cos x \cos y$ set with $B_{str,lim} = 8$ μT and (f) A quadrupole coil from the $\sin x \sin y$ set with $B_{str,lim} = 20$ μT.

in the optimization, this operation is performed by taking the discrete Fourier transform of the rotated spatial domain potential, which has a finer discretization, to interpolate and determine the rotated Fourier components.

B. Coil Conduction Losses

As alternating current (AC) current flows through coupled transformer windings, the losses in the wire are

$$P_w = \frac{1}{2}\begin{bmatrix}\mathbf{I}_1 & \mathbf{I}_2\end{bmatrix}\begin{bmatrix}R_{11} & 0 \\ 0 & R_{22}\end{bmatrix}\begin{bmatrix}\mathbf{I}_1^* \\ \mathbf{I}_2^*\end{bmatrix} \tag{31}$$

where $\mathbf{I}_1$ and $\mathbf{I}_2$ are the current phasors of the primary and secondary coils respectively [20]. In inductive power transfer, the relative phase shift between the current in the windings will be near 90° such that the mutual resistance terms are neglected. This leaves only the self-resistance of the coils, R_{11} and R_{22}.

The increase in self-resistance of a conductor carrying AC is comprised of two effects: the skin effect and the proximity effect. The skin effect is caused by the change in the magnetic field within the conductor due to the change in current within that wire as in Ampere's Law and is characterized by the skin depth

$$\delta_s = \sqrt{\frac{\rho}{\pi\mu f}} = \sqrt{\frac{2\rho}{\omega\mu}} \tag{32}$$

which is defined as the depth in which the field and current density in the conductor falls to e^{-1} of its initial value at the surface of a conductor with resistivity ρ and permeability μ when conducting AC at frequency $\omega = 2\pi f$.

Given the crowding of the current and the associated increase in current density, the skin depth is used in the calculation of the total AC resistance of WPT coil conductors due to the skin effect. For an individual circular conductor with a ratio of strand diameter d_{str} and skin depth δ_s the ratio $F_R(\zeta) = r_s/r_{DC}$ is

$$F_R = \frac{\zeta}{2\sqrt{2}}\left(\frac{\mathrm{ber}_0(\zeta)\mathrm{bei}_1(\zeta) - \mathrm{ber}_0(\zeta)\mathrm{ber}_1(\zeta)}{\mathrm{ber}_1(\zeta)^2 + \mathrm{bei}_1(\zeta)^2} - \frac{\mathrm{bei}_0(\zeta)\mathrm{ber}_1(\zeta) + \mathrm{bei}_0(\zeta)\mathrm{bei}_1(\zeta)}{\mathrm{ber}_1(\zeta)^2 + \mathrm{bei}_1(\zeta)^2}\right) \tag{33}$$

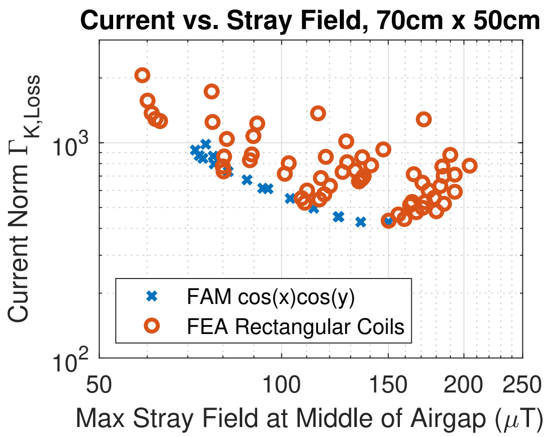

(a)

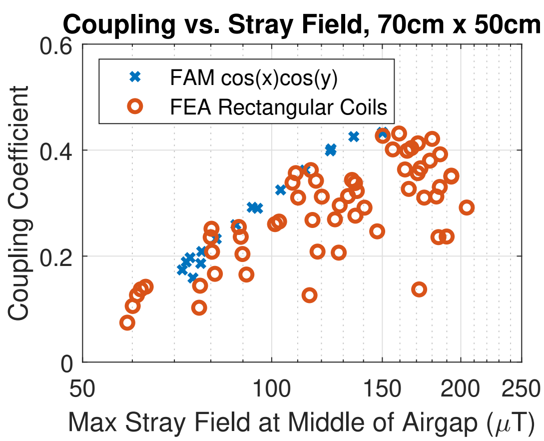

(b)

Fig. 10. Comparison of the $\cos x \cos y$ FAM outputs from the 70 cm $\times$ 50 cm optimization with a sweep of rectangular coils: The stray field maximum at the middle of the airgap taken at $x_{meas} = 0.8$ m and $y_{meas} = 0.6$ m vs. (a) the current norm at 6.6 kW and (b) coupling coefficient at $z_{gap} = 200$ mm at alignment.

where

$$\zeta = \frac{d_{str}}{\sqrt{2}\delta_s} \tag{34}$$

as derived in [21], [22], where r_s is the AC resistance of a circular strand of wire including skin effect and r_{DC} is the DC resistance. Equation (33) is comprised of Kelvin functions that separate the real and imaginary parts of the value of Bessel functions of the first kind $\mathrm{J}_v(\cdot)$ of order v with complex argument $j^{3/2}x$ as in

$$\mathrm{J}_v(j^{3/2}x) = \mathrm{ber}_v(x) + j\,\mathrm{bei}_v(x). \tag{35}$$

Due to the skin effect, the resistance of solid conductors increases rapidly with frequency. Therefore, in this work, Litz wire is used to reduce the AC resistance relative to solid wire. Litz wire is comprised of fine, insulated strands bundled together. When these strands are around or less than a skin depth in diameter, the impact of skin effect can be reduced at cost of decreased packing factor and increased cost. The comprehensive comparison and selection of Litz wire stranding as was done in [23] integrated into FAM is left for future work and Litz wire with 40 AWG strands are used in this work based on availability. Within a circular Litz wire cable, there are n conductors of diameter d_{str}. Once F_R is computed, the total resistance of the Litz wire including skin effect and DC-resistance, R_s, is

$$R_s = \left(\frac{r_{DC} \cdot F_R(\zeta)}{n}\right) L_T \cdot 1.015^{N_b} \cdot 1.025^{N_c} \tag{36}$$

where r_{DC} is the resistance of one strand in the Litz wire per unit length and n is the total number of parallel strands. Here L_T is the total length of wire in the coil multiplied by additional factors to account for the additional length of each conductor due to the number of bundling operations N_b and number of cabling operations N_c as given in the manufacturer datasheet [24].

Losses also occur due to the effect of external fields from conductors near each other, known as the proximity effect. For Litz wire, this is subdivided into two primary categories: internal proximity effect losses and external proximity effect losses. The increase of resistance from these two effects are governed by the factor G_R as defined in (37) which is a function of ζ derived in a similar fashion to F_R [21], [22].

$$G_R = -\frac{\zeta\pi^2 d_{str}^2}{\sqrt{2}} \left(\frac{\mathrm{ber}_2(\zeta)\mathrm{ber}_1(\zeta) + \mathrm{ber}_2(\zeta)\mathrm{ber}_1(\zeta)}{\mathrm{ber}_0(\zeta)^2 + \mathrm{bei}_0(\zeta)^2} + \frac{\mathrm{bei}_2(\zeta)\mathrm{bei}_1(\zeta) - \mathrm{bei}_2(\zeta)\mathrm{bei}_1(\zeta)}{\mathrm{ber}_0(\zeta)^2 + \mathrm{bei}_0(\zeta)^2}\right) \tag{37}$$

Internal proximity effect losses occur within Litz wire cables because the magnetic field generated from the total current within the cross section of the cable varies the distribution of current within individual strands, increasing radially from center of the cable. The strands are bundled and cabled to vary the position of each strand over the length of Litz wire. The external proximity effect is due to the effect of the total field of the coil on each section of a conductor. For ferrite-backed coils with a non-zero gap between the ferrite and windings, the external field $\vec{H}_e$ is the field on each section of the wire. The cross-product of this and the wire direction yields the field orthogonal to the winding section direction unit vector $\hat{dr}$. This includes all H_z components, as the coils are assumed to be in the x-y plane, and H_x and H_y components depending on the direction of the section of wire [12]. The fields are calculated by FAM by (14)-(16). The result of this line integration of the field along the coil contours of the wire is taken and normalized by the RMS current in the wire, I_1 or I_2, to yield the external proximity effect resistance. The summation of these two terms yields the total increase in resistance due to the proximity effect for Litz wire with outer diameter d_o,

$$R_{prox} = n \cdot r_{DC} \cdot G_R(\zeta) \cdot 1.015^{N_b} \cdot 1.025^{N_c} \cdot \left(\oint |\vec{H}_e \times \hat{dr}|^2 / I_1^2 + \frac{1}{2\pi^2 d_o^2} L_T\right). \tag{38}$$

An example of the coil contours and fields used to compute (38) for $I_1 = 17.3$ A is given in Fig. 12. The external fields and direction of each section of wire are calculated with an interpolation of the field values calculated by the FAM to determine orthogonal field components. Once the resistance increases due to the skin effect and proximity effect

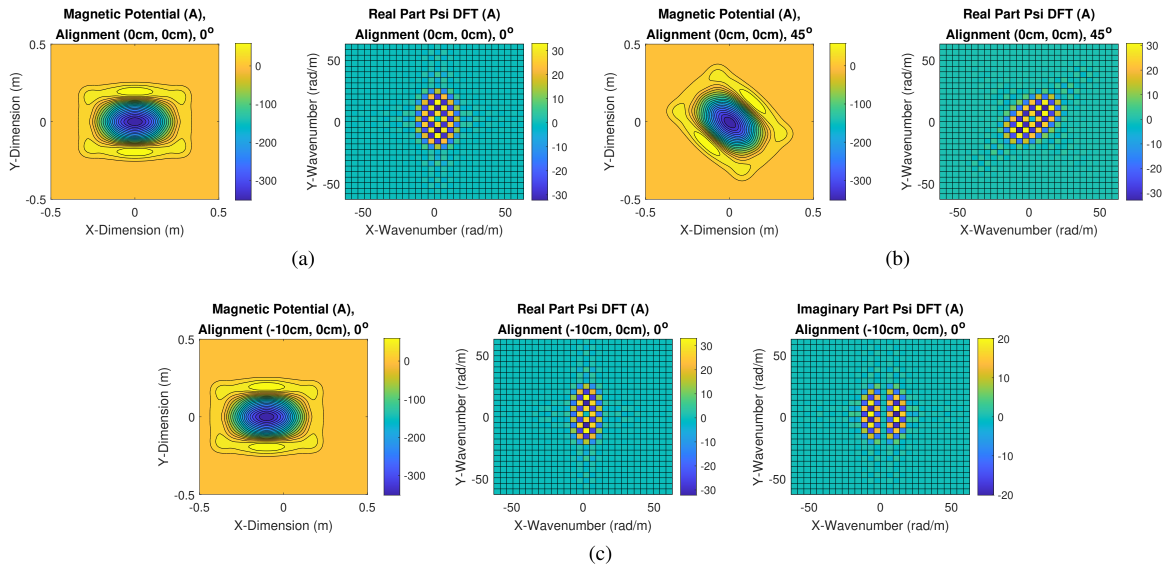

Fig. 11. Magnetic scalar potential under different misalignment cases. (a) Magnetic potential and DFT when aligned. (b) Magnetic potential and DFT with rotational misalignment of 45°. (c) Magnetic potential and DFT with translational misalignment of -10 cm in the x-direction.

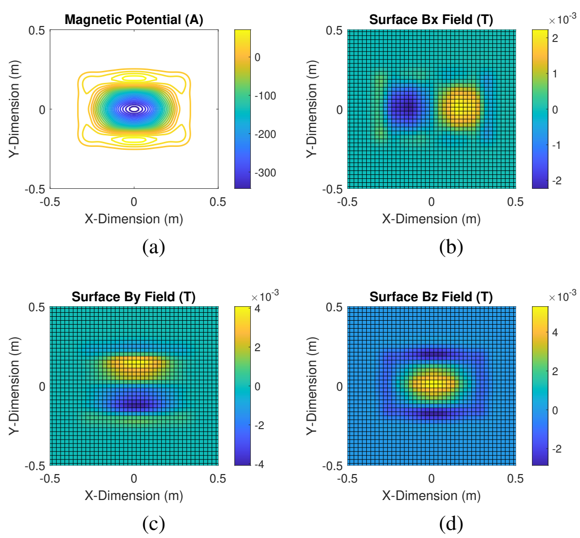

Fig. 12. Example of the coil contours and fields used to calculate external proximity effect loss in FAM. (a) Contours of the magnetic scalar potential of the prototype coil. Surface fields of the coil with a current of 17.3 A in the (b) x-direction, (c) y-direction, and (d) z-direction.

are calculated, the total AC resistance of each coil at a given frequency, R_{11} and R_{22}, are found by the addition of R_s and R_{prox}.

This methodology is used to determine the AC resistance of Litz wire coils with complex geometries. In each case, the overall length of Litz wire and the total external proximity effect is conveniently determined by a line integral of the conductor contours. The orthogonal external fields along the contours are interpolated from the field calculations in (14)-(16) without the need for 3D FEA simulation.

C. Ferrite Losses

Losses in soft-magnetic materials are primarily broken down into hysteresis loss and conduction losses. However, the resistivity of ferrite materials is high, on the order of 5 Ωm, such that the eddy currents in the material are neglected. The Steinmetz equation

$$P_{fe} = C_m f^{\alpha} B_p^{\beta} (T_{fer}^2 C_{t2} - T_{fer} C_{t1} + C_{t0}) \tag{39}$$

is used as a curve-fit of hysteresis loss plots within certain ranges where C_m, α, and β are curve-fit coefficients, P_{fe} is the specific hysteresis loss of the material, and B_p is the peak flux density in the material. The Steinmetz equation is used as the coil currents and flux densities are highly sinusoidal and the flux densities in the ferrite are well under the saturation flux density of the material. The losses are also a function of ferrite temperature, T_{fer} with curve fit parameters C_{t0}, C_{t1}, and C_{t2}. The Steinmetz equation coefficients for the Ferroxcube 3C95 ferrite are summarized in Table II [25]. Many ferrite materials have lower losses when operating at temperatures well above room temperature. For Ferroxcube 3C95, an operating temperature of 25°C increases the loss by 16% relative to the nominal level given by the Steinmetz parameters at 85°C.

To evaluate (39), the spatial flux density in the ferrites must be calculated. In the Fourier Analysis Method, this is conveniently done by taking the integral of each field component to the distance of $\mu_{fer} t_{fer}$ in the z-direction to yield the average flux density in the ferrite of a thickness of t_{fer} and relative permeability μ_{fer}. For a coil in the x-y plane, the average flux density in each direction are

$$B_{x,fer}(x,y) = \sum_{m,n=-N+1}^{N-1} \sum^{N-1} \frac{-\mu_0 j k_x \psi(m,n) e^{j(k_x x + k_y y)}}{\gamma t_{fer}} \cdot (1 - e^{-\gamma t_{fer} \mu_r}) \tag{40}$$

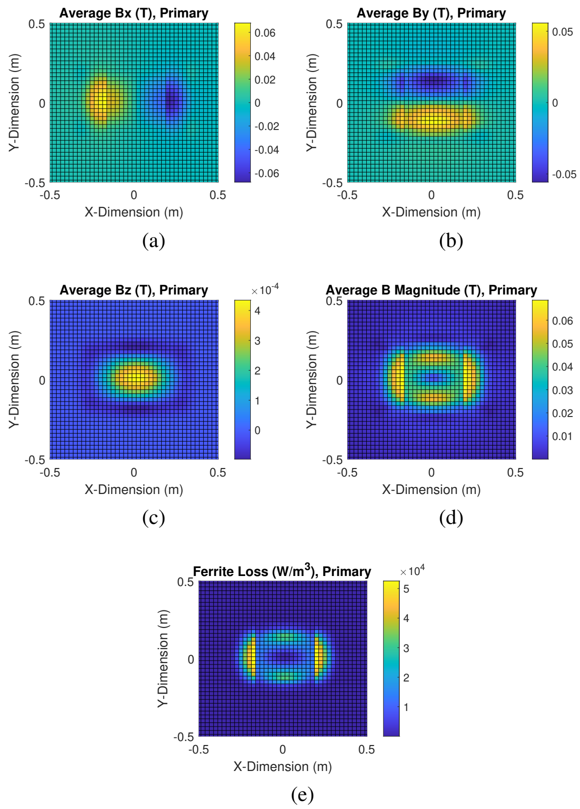

Fig. 13. (a) Average RMS fields in primary ferrite coil with a current of 17.3A in the (a) x-direction, (b) y-direction, and (c) z-direction. (d) The RMS magnitude of the ferrite flux. (e) The spatial specific power loss of the primary coil ferrite at 85 kHz. Here the inner ferrite is 5 mm and the outer ferrite is 2.7 mm, leading to lower peak fields and lower specific power loss in the middle section.

$$B_{y,fer}(x,y) = \sum_{m,n=-N+1}^{N-1}\sum^{N-1} \frac{-\mu_0 j k_y \psi(m,n) e^{j(k_x x + k_y y)}}{\gamma t_{fer}} \cdot (1 - e^{-\gamma t_{fer}\mu_r}) \quad (41)$$

$$B_{z,fer}(x,y) = \sum_{m,n=-N+1}^{N-1}\sum^{N-1} -\mu_0 \psi(m,n) e^{j(k_x x + k_y y)} \cdot (1 - e^{-\gamma t_{fer}\mu_r}). \quad (42)$$

Then the average peak flux density in the ferrite, $B_{avg,fer}(x,y)$, is computed as the vector sum of the field components.

$$B_{avg,fer}(x,y) = \sqrt{(B_{x,fer}(x,y))^2 + (B_{y,fer}(x,y))^2 + (B_{z,fer}(x,y))^2} \quad (43)$$

An example of this calculation is seen in Fig. 13 for the prototype coil in Fig. 15(b) with a primary current of 17.3 A at 85 kHz. In this coil, two different thicknesses of ferrite were used: 2.7 mm on the outside and 5 mm on the inside. This leads to lower flux density and less loss in the middle of the coil, where there is more flux compared to the outside, while reducing the overall weight of ferrite similar to the approach of [11]. The variable ferrite thickness of the prototype is chosen by available ferrite core dimensions and the flux density of the chosen coil geometry.

TABLE II
LOSS MODEL PARAMETER DEFINITIONS AND VALUES

Parameters		Value
Ferrite Steinmetz Parameters Ferroxcube 3C95		$\mu_r = 3000$ $C_m = 92.1\text{e-3 mW/cm}^3$ $\alpha = 1.045$ $\beta = 2.440$
Ferrite Temperature Coefficients Ferroxcube 3C95		$C_{t0} = 1.332$ $C_{t1} = 0.0079$ $C_{t2} = 4.62\text{e-5}$
Steady-State Temperature of Ferrite		$T_{fer} = 20°\text{C}$
Ferrite Thickness		$t_{fer} = 2.7$ mm (outer) $t_{fer} = 5$ mm (inner)
Litz Wire	Outer Diameter Number of Strands Strand Diameter Operations Wire Length	$d_{out} = 3.8$ mm $n = 1100$ $d_{str} = 0.0787$ mm $N_b = 1$ $N_c = 2$ $L_T = 29.8$ m
Compensation Capacitor		$\tan\delta$ see Fig. 14
Inverter On-Resistance NVHL040N120SC1		$R_{DS} = 45$ mΩ
Diode Model Curve Fit STPSC40H12CWL		$V_f = 0.913$ V $R_f = 36.6$ mΩ /2
Temperature Coefficient, Copper		$C_{Cu,t} = +0.393\%/°\text{C}$
Steady-State Temp. of Copper		$T_{Cu} = 38°\text{C}$
Gap Between Ferrite and Wire Plane		$z_g = 7.5$ mm

D. Inverter and Rectifier Losses

In the WPT system, a high-frequency full-bridge inverter drives the primary resonant tank. The secondary side is connected to a full-wave diode rectifier. In a full-bridge inverter, the primary RMS current I_1 will flow through two device on-state resistances R_{DS} for most of the switching period. Therefore, the conduction loss of the switching devices is

$$P_{R_{DS}} = 2 I_1^2 R_{DS}. \quad (44)$$

The switching losses of the inverter are minimized by operating slightly above resonance so that the inverter is soft-switching. Therefore, the switching losses of the inverter and dynamic effects on R_{DS} are not included.

Likewise, on the secondary side, the secondary RMS current I_2 will flow through the forward voltages of the diodes V_f and diode resistances R_f of the rectifier. The reverse-recovery losses of the diodes are negligible as Schottky diodes are used.

$$P_{diode} = 2 V_f I_{2,avg} + 2 I_2^2 R_f \quad (45)$$

The average diode forward current is calculated by

$$I_{2,avg} = \frac{2\sqrt{2}}{\pi} I_2. \quad (46)$$

E. Compensation Component Losses

Power capacitors such as the ones used in the WPT system are designed to have low series resistance and dielectric loss. The ratio of real power, or loss in this case, to reactive power is

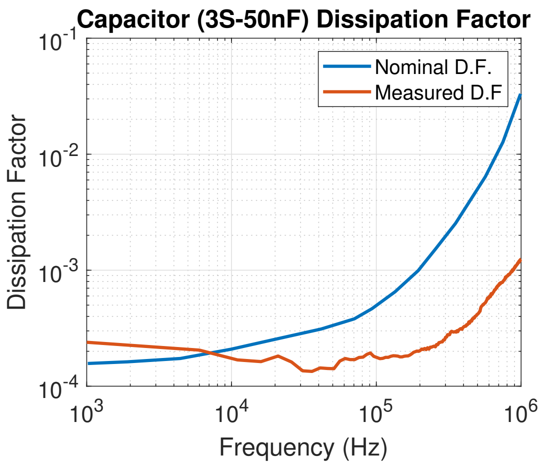

Fig. 14. The frequency-dependent loss tangent of polypropylene (PP) capacitors as in [26] compared to the measured DF of the HC1 capacitor bank with 3, 50 nF capacitors in series.

expressed as the tangent of the angle ϕ of the vector sum of the real power loss P_c and reactive power Q_c in the capacitor, or the dissipation factor (DF). The real power loss of resonant capacitors is comprised of both dielectric and conduction losses. For polypropylene-based capacitors, the dielectric component of the dissipation factor remains constant with frequency at around 10^{-4} to 2×10^{-4}. The conduction loss component of the loss tangent, however, scales with frequency such that the total loss tangent increases with frequency as illustrated in Fig. 14. Here, the measured dissipation factor of the capacitors is about half of the nominal curve given by the manufacturer at 85 kHz. The equivalent series resistance (ESR) of the resonant capacitors R_C and the total power loss P_c are

$$R_C = \frac{\tan \phi(f)}{\omega C} \tag{47}$$

$$P_c = I_1^2 R_{C1} + I_2^2 R_{C2} \tag{48}$$

F. Series-Series System Circuit Model

With an equivalent AC load resistance on the secondary side R_L, the fundamental frequency model of a pair of series-tuned WPT coils is

$$\begin{bmatrix} V_1 \\ 0 \end{bmatrix} = \begin{bmatrix} Z_1 & -j\omega M \\ -j\omega M & Z_2 \end{bmatrix} \begin{bmatrix} I_1 \\ I_2 \end{bmatrix}. \tag{49}$$

where the primary and secondary lumped series impedances are, respectively

$$Z_1 = 2R_{DS} + R_{C1} + R_{11} + j\omega L_1 + 1/(j\omega C_1) \tag{50}$$

$$Z_2 = 2R_f + R_{C2} + R_{22} + R_L + j\omega L_2 + 1/(j\omega C_2). \tag{51}$$

The AC input voltage V_1 and the equivalent AC load resistance R_L are found by the first-harmonic approximation of a square wave as a function of the DC input voltage $V_{1,DC}$ and the DC output load resistance $R_{L,DC}$.

$$R_L = \frac{8}{\pi^2} R_{L,DC} \tag{52}$$

$$V_1 = \frac{4}{\pi} V_{1,DC} \tag{53}$$

Likewise, the DC output voltage is

$$V_{2,DC} = \frac{\pi}{2\sqrt{2}} I_2 R_L - 2V_f. \tag{54}$$

In this linear circuit model, the resistances due to the ferrite losses are neglected. In the final loss calculation, the ferrite losses are calculated from the currents found by this linear model. By inverting this matrix, the input impedance of the system seen by the inverter is

$$Z_{in} = \frac{Z_1 Z_2 + (\omega M)^2}{Z_2}. \tag{55}$$

To ensure zero-voltage switching of the inverter switches, the frequency and load of the WPT system are chosen so that the input impedance of the primary coil is inductive by choosing an operating frequency slightly greater than the resonant frequency of the tanks.

Using the output geometries derived from the optimization for a given $B_{str,lim}$ constraint, the loss and misalignment models detailed in this work are used to analyze efficiency for various conductor types, ferrite thicknesses, and number of turns. As an example, the two geometries in Fig. 16(a)-16(b) from the 70 cm x 50 cm optimization are selected for further analysis. These are the optimization outputs where $B_{str,lim} = 100$ μT for the $\cos x \cos y$ and the $\sin x \cos y$ basis functions. These two solutions were selected because they have the two lowest currents of the four basis function outputs. By varying the number of turns, the impedance of the coils is tuned to meet input voltage requirements with series-series compensation in Fig. 16(c)-16(d). Using the loss models, the efficiencies at alignment are given in Fig. 16(e)-16(f). Here, more turns with higher voltages and lower currents are more efficient than having fewer turns with higher currents mostly due to the reduction of switching device conduction losses as a function of current. Here, it is assumed that the inverter and rectifier have constant device on-state resistances and forward voltages. Solutions with thicker gauges of wire and higher turns are limited by (7) so that the conductors fit in a single layer.

IV. Experimental Results

A 6.6 kW prototype was built to evaluate one of the candidate coil geometries in Fig. 12(a) and validate the loss and field models with experimental measurements. The $\cos x \cos y$ geometry was chosen because it had the lowest loss metric of the four basis function sets at the moderate to large stray field constraints. The parameters used to model the system performance are given in Table II. The overall system consists of a set of two matched planar coils, two compensation capacitor banks, and power electronics consisting of a full-bridge inverter with four MOSFETs and gate driver boards, a control board with an FPGA, and a full-bridge diode rectifier as in Fig. 15(a).

One of the two identical prototype coils is shown in Fig. 15(b). Each coil is a sandwich structure comprised, from top to bottom, of a polycarbonate coil former with litz wire,

This article has been accepted for publication in IEEE Transactions on Transportation Electrification. This is the author's version which has not been fully edited and content may change prior to final publication. Citation information: DOI 10.1109/TTE.2024.3363612

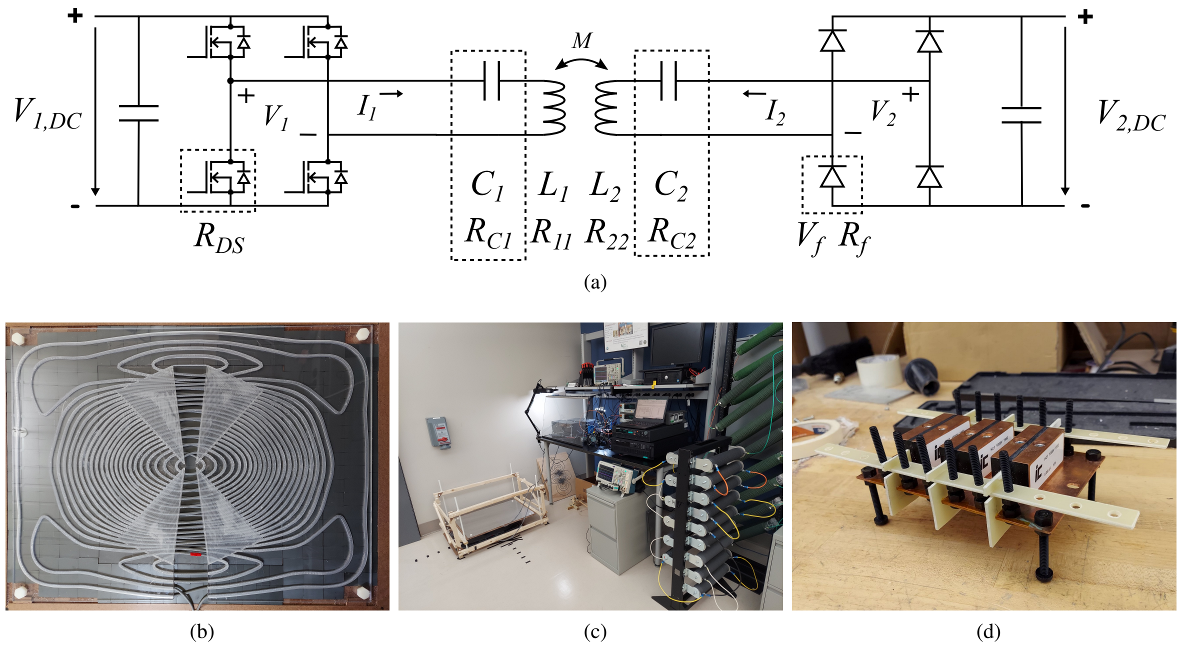

Fig. 15. (a) Schematic of the overall setup with inverter, resonant capacitors, coils, and rectifier. (b) Prototype 6.6 kW coil. (c) Overall experimental setup. (d) Resonant capacitor bank.

ferrite tiles of two thicknesses, hardboard spacers, and an aluminum sheet held together with nylon bolts and reinforced tape. The total length of the wire in each coil was measured to be 29.8 m, with 24.8 m in the coils themselves. The calculated length of the contours was 24.8 m. The additional lead length needed to connect to the inverter, capacitors, and rectifier is accounted for in the loss model. The airgap holder in Fig. 15(c) was made out of wood and nylon bolts to suspend one of the coils at different airgaps. The four threaded nylon rods allow for the quick adaptation of the airgap and support the upper coil from the bottom. Litz wire was used to symmetrically wind the coils.

The compensation capacitors are constructed of high-density resonant capacitors from Illinois Capacitor. Due to the need to reach high voltage levels, three capacitors were placed in series as seen in Fig. 15(d). An identical bank was constructed and connected to the secondary side to provide series-series tuning for the system. The area between the nuts on the underside of the capacitors required additional voltage insulation where the corners of nuts were facing each other. To resolve this issue, FR4 fins placed on top of Mylar tape were made to provide additional voltage insulation between the capacitor nuts. These are held in place by long pieces of FR4 aligning the busbars and nylon bolts. The assembly is enclosed in a PVC and plexiglass box.

A. Impedance Measurements

In Table III, the measured and calculated inductances of the system are compared. The measurements were obtained with an Agilent Technologies E4990A impedance analyzer. As measured, the self-inductance of the coils change as a function of airgap due to the presence of ferrite across the airgap as also seen in [27]. The FAM model also captures this effect. This change in self-inductance slightly changes the resonant frequency of the tank. To account for this effect, the operating frequency is chosen such that the input impedance is inductive for the largest airgap, when the coil self-inductances are lowest and the tank resonant frequency is the highest. The airgap used in this document is defined as the magnetic airgap of the system, i.e. the distance between the ferrites of each coil.

In Fig. 17, the measured series impedances of the primary and secondary tanks are shown when tuned to the 86.5 kHz operating points with three 50 nF capacitors in series. The parasitic parallel resonances of the tanks were seen to produce a high-frequency resonant current, as seen in the later test results. This high frequency current produces a negligible additional loss not captured in the fundamental frequency loss models.

B. Finite-Element Analysis Simulation of the Prototype

The physical prototype was implemented with litz conductors, a finite ferrite sheet close to the size of the coil extents, and an aluminum backing sheet. The aluminum sheet is used in the prototype for structural support and backside shielding and extends 1 cm on all sides beyond the outer ferrite extents. These non-ideal elements were included in an FEA simulation of the prototype to determine if they have any effect on the estimated impedance or fields relative to the FAM-derived values. The contours of the coil geometry were exported to finite-element analysis (FEA) software to accomplish this.

In Fig. 18, the FEA outputs of prototype fields are plotted with and without the aluminum sheet. As seen, the aluminum sheet provides some additional shielding for the fields far away from the coils at 80 cm, while the larger fields near the coils in the airgap are not significantly altered. The fields on the backside of the ferrite are also shielded by the aluminum sheet. This is similar to the result of [28] for unipolar coil shielding by aluminum sheets, though not as significantly as

TABLE III
CALCULATED INDUCTANCE VALUES VS. MEASUREMENTS

Airgap	Param.	FEA	FAM	Measured	FEA Error (%)	FAM Error (%)
125 mm	L_1, L_2	216.1 μH	224.9 μH	218.9 μH, 217.2 μH	-1.3%, -0.5%	2.7%, 3.5%
	M	75.2 μH	82.6 μH	79.9 μH	-5.9%	3.4%
210 mm	L_1, L_2	203.2 μH	204.5 μH	205.4 μH, 203.8 μH	-1.1%, -0.3%	-0.4%, 0.3%
	M	29.8 μH	31.9 μH	30.2 μH	-1.3%	5.6%
250 mm	L_1, L_2	201.7 μH	201.7 μH	200.3 μH, 199.7 μH	0.7%, 1.0%	0.7%, 1.0%
	M	20.3 μH	21.7 μH	20.0 μH	1.5%	8.5%

the aluminum and ferrite are similarly sized. The FEA-derived inductance values are also compared with the FAM and measured values in Table III. Regarding mutual inductance, the FAM calculation method tends to slightly overestimate mutual inductance relative to FEA and the measured values at larger airgaps such as 210 mm and 250 mm. This is likely due to the homogenous boundary conditions used in FAM modeling, which approximates a large, continuous ferrite sheet. This error may become worse at larger airgaps as the coupled fields spread out. In contrast, the FEA simulations include finite ferrite dimensions and tend to underestimate mutual inductance at lower airgaps. As shown, the FAM and FEA derived inductance values both match the measured values with a maximum absolute error of 8.5% and 5.9%, respectively. FEA airgap fields also match the FAM-derived and measured values in Fig. 21.

C. *Efficiency Measurements and Waveforms*

Tests were run to validate the efficiency and loss models over misalignment. Two power supplies were used in the tests: a Keysight N8935A for the high-power tests at 125 mm at 3.4 kW and 210 mm at 6.7 kW at alignment and a BK Precision PVS60085MR for the other low-power tests. A BK Precision 8612 electronic load was used alone or in parallel with wirewound resistors for these low-power tests. For the high-power tests, the wirewound resistor bank alone was used. Because of the voltage and current limitations of the electronic load and power supply for the low-power tests, the power levels are limited to 1.1 kW and below at 250 mm and at 125 mm and 210 mm in misaligned conditions. The system waveforms were obtained with a Tektronix MSO4104B-L. The DC current and voltage measurements used to derive DC-DC efficiency were obtained by multimeter and power supply current measurements. For these tests, the system was run in open-loop with constant load resistance.

The waveforms of the system at 210 mm and 6.7 kW are shown in Fig. 19(a). The frequency components of the waveforms are also given in Fig. 19(b)-19(c), showing the square-wave harmonics of the inverter and rectifier voltages and coil currents. The effect of the parasitic resonances of the tanks in Fig. 17 is seen in high-frequency components of the current waveforms. At the 6.7 kW operating point, the temperatures of the system elements were captured by thermal camera as shown in Fig. 19(d)-19(e). These temperatures were used to determine the temperatures used in the loss models in Table II. As seen, due to the 6.6 kW power level and high efficiency of the system, the wire temperature only rose 19°C above ambient with no active cooling. This temperature was used in the loss models to estimate the wire loss. The modeled loss breakdown of the system and efficiency measurements over varying misalignments are shown in Fig. 20. In these figures, the loss models matched the experimental measurements well over varying misalignments.

TABLE IV
PEAK MEASURED DC/DC EFFICIENCIES AT 86.5KHZ

Airgap	Misalignment (X,Y)			
	0 cm, 0 cm	-10 cm, 0 cm	0 cm, -7.5 cm	45°
125 mm	97.6%	96.6%	96.3%	97.0%
210 mm	95.6%	94.0%	93.0%	94.5%
250 mm	93.1%	91.4%	90.9%	92.4%

TABLE V
SENSOR CUBIC VALUES

Parameter	Value	
Magnet Wire AWG	30 AWG	
Number of Turns	$N_T = 45$ turns	
Turn Area	$A = 23.04$ cm^2	
Field Sensitivity (dV/dB)	86.5 kHz	56.4 mV/μT
RC Filter Values	$R =$1.6 kΩ $C = 300$ pF	
RC Corner Frequency	300 kHz	

A summary of the measured efficiency values is given in Table IV. As shown, the efficiency of this work is similar to the previous works summarized in Table VII when compared by the airgap divided by the geometric mean length (GML) of the coil dimensions similar to the metric proposed in [29].

D. *Field Measurements*

A sensor cubic similar to [5] was made to measure the fields of the system during operation for comparison with model values. The voltages induced in the sensor windings were measured with a Tektronix MDO3104 oscilloscope. Due to the high-frequency self-resonance of the sensor windings, an RC filter was used to damp the high-frequency voltages and is included in the calculation of the stray field. The parameters of the cubic and RC-filter are given in Table V. Field measurements at the center of a 210 mm airgap are shown in Fig. 21. Here, the FAM field models match the experiment with some accuracy, especially for the B_z values.

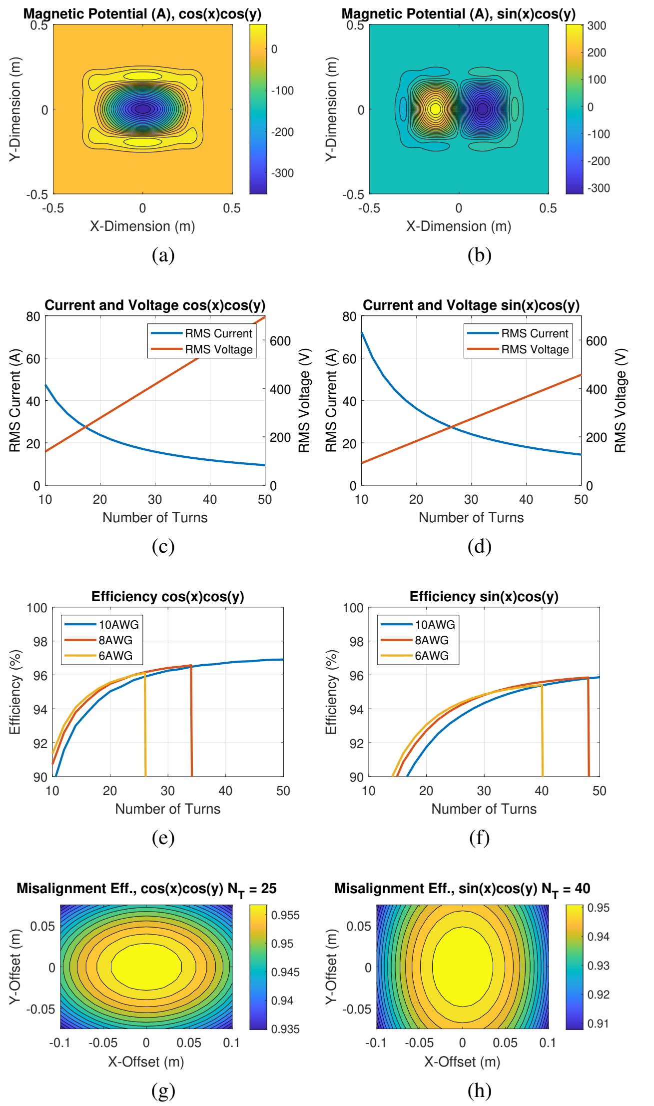

Fig. 16. Points from the 70 cm x 50 cm optimization shown for with $B_{str,max} = 100\mu$T, $f = 85$ kHz, $z_{gap} = 210$ mm, and $P = 6.6$ kW and modeled loss using the parameters of Table II. (a) Potential of the $\cos x \cos y$ coil geometry. (b) Potential of the $\sin x \cos y$ coil geometry. Current and voltage for the (c) $\cos x \cos y$ coil geometry and the (d) $\sin x \cos y$ coil geometry. Efficiency at alignment of the (e) $\cos x \cos y$ coil geometry and the (f) $\sin x \cos y$ coil geometry from the loss models in this paper where $I_1 = I_2$. Misalignment efficiency of the (g) $\cos x \cos y$ coil geometry with $N_T = 25$ and the (h) $\sin x \cos y$ coil geometry with $N_T = 40$ with $I_1 = I_2$.

The B_x and B_y values were affected by the accuracy of positioning the sensor cubic height between the coils. These measurements were taken at a DC output power of 474 W to limit the voltages induced in the sensor windings from the large fields within the coil extents. The measurements are scaled by the square root of the ratio of 6.6 kW to 474 W.

The measured stray fields at 80 cm are summarized in Table VI. The field measurements at misalignment are on the side closest to the misaligned secondary. Compared to the literature on a normalized basis of stray field divided by the square root of output power, the measured stray fields at 80 cm were less than the works summarized in Table VII and well below the ICNIRP 27 µT and 15 µT pacemaker

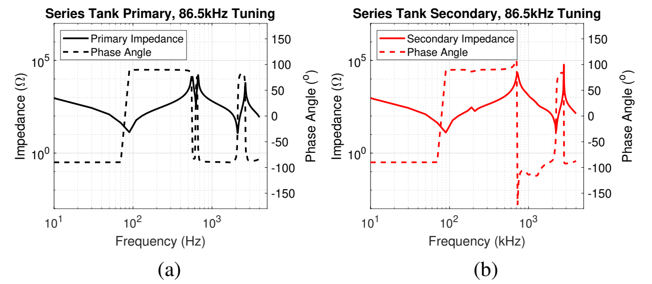

Fig. 17. Tank Impedance of the (a) primary and (b) secondary tanks at 86.5 kHz tuning.

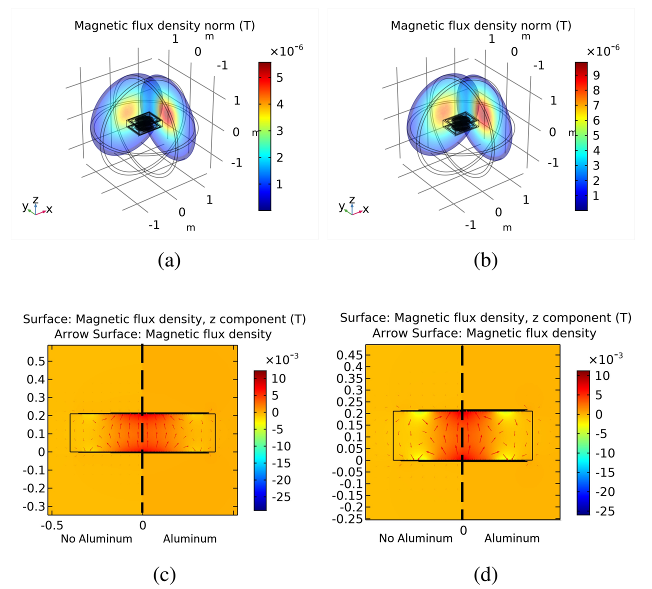

Fig. 18. FEA Outputs for the prototype coil with RMS currents I_1 =21.3 A and I_2 =18.6 A. (a) Peak stray fields at 80 cm with aluminum sheet. (b) Peak stray fields at 80 cm without aluminum sheet. (c) Peak B_z fields in the X-Z plane at $y = 0$ with and without aluminum sheet. (d) Peak B_z fields in the Y-Z plane at $x = 0$ with and without aluminum sheet.

limits. In Table VII, the stray field metric µT/kW$^{0.5}$ comes from the direct relationship between the coil currents and field magnitude and the coil to coil power equation, $P = \omega M I_1 I_2$, where the power is proportional to the product of the coil currents. This relationship allows the stray fields of systems operating at different power levels to be compared and for the scaling of stray field measurements to higher or lower power levels as done in this work.

V. Conclusion

In this work, the Fourier Analysis Method (FAM) was used to predict the system efficiency, inductances, fields, and performance of complex, symmetric planar coil geometries derived from an optimization of Fourier basis function coefficients. The optimization outputs are geometries that meet the stray field and power level constraints with minimized loss factors. The FAM is then used to estimate the efficiency over various number of turns, conductor sizes, and ferrite thicknesses over varying airgaps and misalignments. As shown, the Fourier representation of the coil geometry also enables the convenient

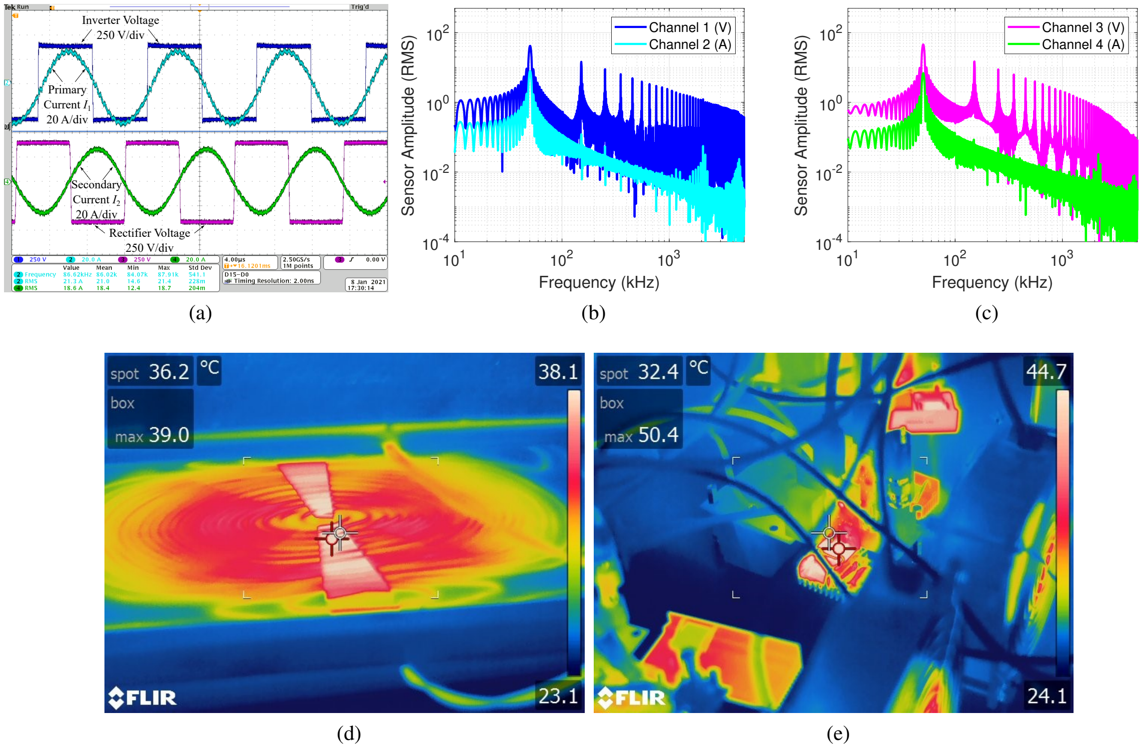

Fig. 19. Experimental results at 6.7 kW and 86 kHz, 210 mm at alignment. (a) Waveforms of switch node voltages and currents. CH1: Blue primary switch node voltage (250 V/div), CH2: cyan primary current I_1 (20 A/div), CH3: magenta secondary switch node voltage (250 V/div), and CH4: green secondary current I_2 (20 A/div). (b) Frequency components of CH1 and CH2. (c) Frequency components of CH3 and CH4. (d) Thermal image of secondary coil showing a maximum wire temperature of 39°C. (e) Thermal image of the inverter (top) and rectifier (bottom) heat sinks.

TABLE VI
SUMMARY OF SCALED RMS FIELD MEASUREMENTS (X,Y) AT 0.8 M, 86.5 KHZ AND 6.6 KW

Airgap	Misalignment (X,Y)		
	0 cm, 0 cm	-10 cm, 0 cm	0 cm, -7.5 cm
125 mm	1.8 μT, 1.4 μT	4.5 μT, 1.8 μT	2.1 μT, 3.1 μT
210 mm	4.4 μT, 3.6 μT	6.6 μT, 4.2 μT	4.5 μT, 5.6 μT
250 mm	6.5 μT, 4.5 μT	8.9 μT, 5.3 μT	6.6 μT, 7.2 μT

calculation of coupling over misalignment, the external field on the conductors in proximity effect loss calculation, and the ferrite flux density for the calculation of ferrite loss for complex coil geometries.

A 6.6 kW WPT prototype with a shielded rectangular coil geometry was built from an optimization output to validate the method. The prototype was tested over a range of misalignments and airgaps to test the inductance, field, and loss models. As shown in Table VII, the prototype achieved similar efficiency with lower stray field when compared to the literature by a metric of the airgap over the geometric mean length (GML) of the coils and a metric of stray field over the square root of output power. Improving the efficiency and stray field is essential to achieve inductive charging for EVs that complies with stray field and EMI limits. In future work, the loss models will be imported into a time-domain simulation platform to assess thermal effects and cooling to design and validate a higher-power WPT system.

ACKNOWLEDGMENT

The authors would like to thank Bob Martin and Caden Webb for their assistance with the material procurement, manufacture, and setup of the experimental system.

REFERENCES

[1] A. Foote, D. Costinett, R. Kusch, J. Pries, M. Mohammad, and B. Ozpineci, "Fourier analysis method for wireless power transfer coil design," in *2020 IEEE 21st Workshop on Control and Modeling for Power Electronics (COMPEL)*, 2020, Conference Proceedings, pp. 1–8.

[2] A. Foote, "Fourier analysis and optimization of inductive wireless power transfer for electric vehicle charging," Ph.D. dissertation, University of Tennessee, 2023.

[3] Society of Automotive Engineers, "J2954: Wireless power transfer for light-duty plug-in/electric vehicles and alignment methodology," 2020. [Online]. Available: https://www.sae.org/standards/content/j2954_202010/

[4] IEC, "CISPR 11: Industrial scientific and medical equipment - Radiofrequency disturbance characteristics - Limits and methods of measurement," June 2016.

[5] R. Bosshard, U. Iruretagoyena, and J. W. Kolar, "Comprehensive evaluation of rectangular and Double-D coil geometry for 50 kW/85 kHz IPT system," *IEEE Journal of Emerging and Selected Topics in Power Electronics*, vol. 4, no. 4, pp. 1406–1415, 2016.

TABLE VII
COMPARISON OF WPT SYSTEMS IN THE LITERATURE AND THE PROTOTYPE

Ref.	Power Level	Coil Dimension	Airgap (mm)	Airgap/ GML	Stray Field 80 cm - X, Y	Stray Field Metric $kW^{0.5}/\mu T$	DC/DC Efficiency	Freq. (kHz)	Coil Shape	Power Density
[5]	50 kW	76 cm x 41 cm	160	(0.29)	N/A, 22.5 μT	(N/A, 0.31)	95.8%	85	Rect.	2.0 kW/kg
[5]	50 kW	76 cm x 41 cm	160	(0.29)	N/A, 12.5 μT	(N/A, 0.57)	95.3%	85	DD	2.0 kW/kg
[9], [30]	120 kW	88 cm x 67 cm	125	(0.16)	19.1 μT, 12.3 μT (11 kW)	(0.17, 0.27)	97.1%	25	DD	2.28 kW/kg
[31]	50 kW	54 cm x 47 cm	150	(0.30)	N/A, 34.7 μT	(N/A, 0.20)	95.1%	85	3Φ-DD	3.65 kW/kg
[32]	3 kW	60 cm O.D.	100 135 170	(0.17) (0.23) (0.28)	N/A	N/A	95.8% 94.2% 92.1%	35	Circular	0.79 kW/kg
This Work	6.6 kW	71 cm x 54 cm	125 210 250	(0.20) (0.34) (0.41)	1.8 μT, 1.4 μT 4.4 μT, 3.6 μT 6.5 μT, 4.5 μT	(1.43, 1.84) (0.58, 0.71) (0.40, 0.57)	97.6% 95.5% 93.1%	86.5	Shielded Rect.	0.81 kW/kg

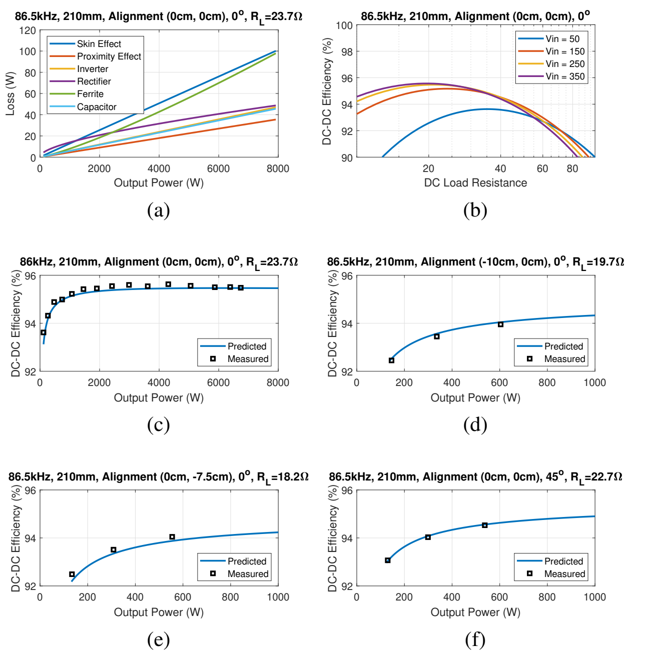

Fig. 20. (a) Modeled loss breakdown of the system at alignment over varying output resistances. (b) Modeled efficiency of system over load resistance at alignment. (c) Model efficiency vs. measured efficiency at alignment, (d) at -10 cm in the x-direction, (e) at -7.5 cm in the y-direction, and (f) at 45°rotation.

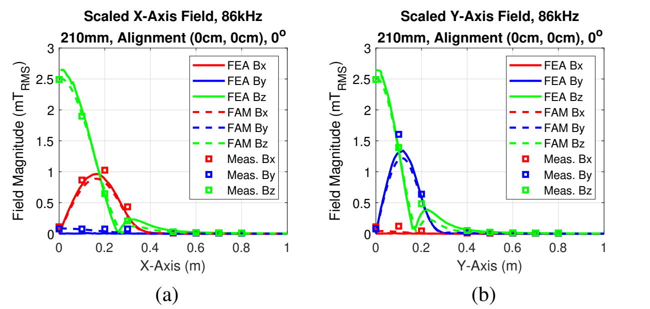

Fig. 21. Scaled field measurements, FEA values, and FAM model outputs at 86 kHz, 210 mm, and 6.6 kW. (a) Fields on the X-axis and (b) the Y-axis.

[6] T. Campi, S. Cruciani, F. Maradei, and M. Feliziani, "Active coil system for magnetic field reduction in an automotive wireless power transfer system," in *2019 IEEE International Symposium on Electromagnetic Compatibility, Signal and Power Integrity (EMC+SIPI)*, 2019, Conference Proceedings, pp. 189–192.
[7] M. Lu and K. D. T. Ngo, "Circuit models and fast optimization of litz shield for inductive-power-transfer coils," *IEEE Transactions on Power Electronics*, vol. 34, no. 5, pp. 4678–4688, 2019.
[8] M. Mohammad, M. S. Haque, and S. Choi, "A litz-wire based passive shield design to limit EMF emission from wireless charging system," in *2018 IEEE Energy Conversion Congress and Exposition (ECCE)*, 2018, Conference Proceedings, pp. 97–104.
[9] M. Mohammad, J. Pries, O. Onar, V. P. Galigekere, G. Su, S. Anwar, J. Wilkins, U. D. Kavimandan, and D. Patil, "Design of an EMF suppressing magnetic shield for a 100-kW DD-coil wireless charging system for electric vehicles," in *2019 IEEE Applied Power Electronics Conference and Exposition (APEC)*, 2019, Conference Proceedings, pp. 1521–1527.
[10] B. Zhang, R. B. Carlson, V. P. Galigekere, O. C. Onar, and J. L. Pries, "Electromagnetic shielding design for 200 kW stationary wireless charging of light-duty EV," in *2020 IEEE Energy Conversion Congress and Exposition (ECCE)*, 2020, Conference Proceedings, pp. 5185–5192.
[11] M. Mohammad, S. Choi, Z. Islam, S. Kwak, and J. Baek, "Core design and optimization for better misalignment tolerance and higher range of wireless charging of PHEV," *IEEE Transactions on Transportation Electrification*, vol. 3, no. 2, pp. 445–453, 2017.
[12] M. Lu and K. D. T. Ngo, "Analytical calculation of proximity-effect resistance for planar coil with litz wire and ferrite plate in inductive power transfer," *IEEE Transactions on Industry Applications*, pp. 1–1, 2019.
[13] G. N. Peeren, "Stream function approach for determining optimal surface currents," Thesis, Eindhoven University of Technology, 2003.
[14] M. Poole, P. Weiss, H. S. Lopez, M. Ng, and S. Crozier, "Minimax current density coil design," *Journal of Physics D: Applied Physics*, vol. 43, no. 9, 2010.
[15] M. Landreman, "An improved current potential method

for fast computation of stellarator coil shapes," *Nuclear Fusion*, vol. 57, no. 4, 2017.

[16] J. R. Melcher, *Continuum Electromechanics*. MIT press Cambridge, 1981, vol. 2.

[17] B. L. J. Gysen, K. J. Meessen, J. J. H. Paulides, and E. A. Lomonova, "General formulation of the electromagnetic field distribution in machines and devices using Fourier analysis," *IEEE Transactions on Magnetics*, vol. 46, no. 1, pp. 39–52, 2010.

[18] Z. Luo and X. Wei, "Analysis of square and circular planar spiral coils in wireless power transfer system for electric vehicles," *IEEE Transactions on Industrial Electronics*, vol. 65, no. 1, pp. 331–341, 2018.

[19] J. P. C. Smeets, T. T. Overboom, J. W. Jansen, and E. A. Lomonova, "Three-dimensional magnetic field modeling for coupling calculation between air-cored rectangular coils," *IEEE Transactions on Magnetics*, vol. 47, no. 10, pp. 2935–2938, 2011.

[20] C. Feeney, J. Zhang, and M. Duffy, "AC winding loss of phase-shifted coupled windings," *IEEE Transactions on Power Electronics*, vol. 31, no. 2, pp. 1472–1478, 2016.

[21] M. K. Kazimierczuk, *High-frequency magnetic components*. John Wiley and Sons, 2009.

[22] J. Mühlethaler, "Modeling and multi-objective optimization of inductive power components," PhD Dissertation, ETH Zürich, Zürich, Switzerland, 2012.

[23] C. R. Sullivan, "Cost-constrained selection of strand diameter and number in a litz-wire transformer winding," *IEEE Transactions on Power Electronics*, vol. 16, no. 2, pp. 281–288, 2001. [Online]. Available: http://ieeexplore.ieee.org/document/911153/

[24] New England Wire, "Litz wire technical information," https://www.newenglandwire.com/, 2003.

[25] Ferroxcube, "Power conversion materials," https://www.ferroxcube.com, 2020.

[26] Illinois Capacitor, "Metallized polypropylene film capacitors data," https://www.illinoiscapacitor.com/, 2020.

[27] S. Y. Jeong, J. H. Park, G. P. Hong, and C. T. Rim, "Autotuning control system by variation of self-inductance for dynamic wireless EV charging with small air gap," *IEEE Transactions on Power Electronics*, vol. 34, no. 6, pp. 5165–5174, 2019.

[28] M. Mohammad, J. L. Pries, O. C. Onar, V. P. Galigekere, G. J. Su, and J. Wilkins, "Comparison of magnetic field emission from unipolar and bipolar coil-based wireless charging systems," in *2020 IEEE Transportation Electrification Conference and Expo (ITEC)*, 2020, Conference Proceedings, pp. 1201–1207.

[29] A. L. Stein, P. A. Kyaw, and C. R. Sullivan, "Figure of merit for resonant wireless power transfer," in *2017 IEEE 18th Workshop on Control and Modeling for Power Electronics (COMPEL)*, 2019, Conference Proceedings, pp. 1–7.

[30] V. P. Galigekere, J. Pries, O. C. Onar, G. Su, S. Anwar, R. Wiles, L. Seiber, and J. Wilkins, "Design and implementation of an optimized 100 kW stationary wireless charging system for EV battery recharging," in *2018 IEEE Energy Conversion Congress and Exposition (ECCE)*, 2018, Conference Proceedings, pp. 3587–3592.

[31] J. Pries, V. P. N. Galigekere, O. C. Onar, and G.-J. Su, "A 50-kW three-phase wireless power transfer system using bipolar windings and series resonant networks for rotating magnetic fields," *IEEE Transactions on Power Electronics*, vol. 35, no. 5, pp. 4500–4517, 2020.

[32] T. Diekhans and R. W. D. Doncker, "A dual-side controlled inductive power transfer system optimized for large coupling factor variations and partial load," *IEEE Transactions on Power Electronics*, vol. 30, no. 11, pp. 6320–6328, 2015.

Andrew Foote (Member, IEEE) received the B.S. degree in electrical engineering from Auburn University, Auburn in 2016 and the Ph.D. degree in electrical engineering from the University of Tennessee, Knoxville in 2023. From 2016-2019, he joined the Power Electronics and Electric Machinery Group at Oak Ridge National Laboratory as a Graduate Research Assistant. In 2020, he joined Volkswagen Group of America at Innovation Hub Knoxville as part of the first cohort of Ph.D. Fellows and transitioned to working as a Research Engineer there in November 2023.

His research interests include the design and optimization of inductive wireless charging assemblies, magnetic components, resonant tank elements, thermal management, power electronic converters, and electric machines and drives for electric vehicles.

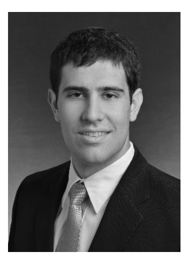

Daniel Costinett (Senior Member, IEEE) received the Ph.D. degree in electrical engineering from the University of Colorado Boulder in 2013. He was an instructor at Utah State University in 2013. Since 2013, he has been with the Department of Electrical Engineering and Computer Science at the University of Tennessee, Knoxville (UTK), where he is currently an Associate Professor. Dr. Costinett is Co-Director of Education and Diversity for the National Science Foundation/Department of Energy Engineering Research Center for Ultra-wide-area Resilient Electric Energy Transmission Networks (CURENT). He has coauthored more than 150 peer-reviewed publications. His research interests include resonant and soft switching power converter design, high efficiency wired and wireless power supplies, on-chip power conversion, medical devices, and electric vehicles.

Dr. Costinett was a recipient of the National Science Foundation CAREER Award in 2017, the 2022 Richard M. Bass Outstanding Young Power Electronics Engineer Award, the 2016 and 2020 IEEE PELS Transactions Second Place Prize Paper Award, and the 2015 IEEE IAS William M. Portnoy Award. He received the 2022 Moses E. and Mayme Brooks Distinguished Professor Award, 2015 ECE Faculty of the Year Award, and 2020 Chancellor's Award for Professional Promise in Research from UTK. He currently serves as Associate Editor of *IEEE Transactions on Power Electronics* and *IEEE Journal of Emerging and Selected Topics in Power Electronics*.

Ruediger Kusch (Senior Member, IEEE) received the Ph.D. degree in electrical engineering from Berlin University of Technology, Germany, in 2006, and the Dipl.-Ing. degree in electrical engineering from the Braunschweig University of Technology, Germany, in 1998, respectively. In 2001/02, he was a research scholar at the Department of Electrical and Computer Engineering, University of Wisconsin (WEMPEC), Madison. From 2006 to 2013 he was with General Electric Global Research, Niskayuna, USA. He is currently a Senior Engineer at Volkswagen R&D, Germany.

His interests include electrical machines and drives and their control. Projects involve electrification of the vehicle drive train, wide bandgap semiconductors, power conversion, electric vehicles, battery management systems, fuel cell systems, more electric aircraft, medium voltage drives, solid state transformer, power converter topologies and high bandwidth control. He is a member of the IEEE and holds 45 patents.

Mostak Mohammad (Senior Member, IEEE) completed his B.Sc. degree in 2009 in electrical and electronics engineering from the Bangladesh University of Engineering and Technology (BUET), Bangladesh, and his Ph.D. in Electrical Engineering in 2019 from the University of Akron, OH, USA. From 2009 to 2014, he worked as a specialist in Radio Network Planning in Robi Axiata Limited, Bangladesh, where he developed radio-frequency propagation models for FEA-based cellular network design.

Dr. Mohammad is currently working as an R&D Associate Staff in the National Transportation Research Center at Oak Ridge National Laboratory. He has been working on high-power (11 kW to 500 kW) single-phase, poly-phase, stationary and dynamic wireless charging systems. His research interests include high-fidelity multi-physics modeling and optimization, high-power wireless charging for electric vehicles, magnetic materials, electromagnetic shielding, and electric machine design.

Omer Onar (Senior Member, IEEE) received his Ph.D. degree in Electrical Engineering from the Illinois Institute of Technology, Chicago, IL, in 2010. In November 2010, he joined the Power Electronics and Electric Machinery Group at the U.S. Department of Energy's Oak Ridge National Laboratory (ORNL), Oak Ridge, TN, USA as a Distinguished Alvin M. Weinberg Fellow.

He is currently leading the Vehicle Power Electronics Research (VPER) Group under the Vehicle and Mobility Systems Research Section, Buildings and Transportation Science Division. His research interests cover power electronic converters for EV charging applications, wireless power transfer systems, bidirectional EV charging systems, and drive systems.